The resting state of the human T-cell receptor–CD3 complex

Ryan Q. Notti[1,2,*], Fei Yi[3,4], Søren Heissel[5], Martin W. Bush[1], Henrik Molina[5], Zaki Molvi[6], Christopher A. Klebanoff[2,3,4], and Thomas Walz[1]

[1] Laboratory of Molecular Electron Microscopy, The Rockefeller University, New York, NY

[2] Department of Medicine, Memorial Sloan Kettering Cancer Center, New York, NY

[3] Human Oncology Pathogenesis Program, Memorial Sloan Kettering Cancer Center, New York, NY

[4] Parker Institute for Cancer Immunotherapy, Memorial Sloan Kettering Cancer Center, New York, NY

[5] Proteomics Resource Center, The Rockefeller University, New York, NY

[6] Immunology Program, Memorial Sloan Kettering Cancer Center, New York, NY

[*] To whom correspondence should be addressed: rnotti@rockefeller.edu

Summary

The T-cell receptor (TCR) is central to the ligand-dependent activation of T lymphocytes and as such orchestrates both adaptive and pathologic immune processes[1]. However, major questions remain regarding the structure and function of the human TCR[2–4]. Here, we present cryogenic electron microscopy structures for the unliganded human TCR–CD3 complex in a native-like lipid bilayer, revealing two related conformations that are distinct from its structure in detergent. These new “closed and compacted” conformations afford insights into the interactions between the TCR–CD3 and the membrane, including conserved surface patches that make extensive outer leaflet contact, and suggest novel conformational regulation by glycans. We show that the closed/compacted conformations, not the extended one previously reported in detergent[5–8], represent the unliganded resting state for the TCR–CD3 *in vivo*, underscoring the importance of

structural interrogation of membrane proteins in native-like environments. We use conformation-locking disulfide mutants to show that ectodomain opening is necessary for maximal ligand-dependent TCR–CD3 activation, demonstrating that TCR-intrinsic conformational change is necessary for full TCR–CD3 activation and opening numerous avenues for immunoreceptor engineering.

Main

T cells are central to a wide array of both adaptive and pathologic immune responses. The T-cell receptor (TCR), in association with members of the CD3 protein family, allows T cells to recognize and respond to antigenic peptides presented on human leukocyte antigen (HLA) complexes of other cells. While the identities of the TCR–CD3 complex constituents and its downstream signaling elements have been known for some time, questions remain regarding its activation mechanism.

The TCR–CD3 is a hetero-octameric membrane protein complex[5–8]. The αβ-type TCR is comprised in part by two variable chains, TCRα and TCRβ, which directly interface with the HLA-antigen complex. Antigen specificity is generated through somatic recombination of the variable segments in the TCRα and TCRβ genes. The remainder of the core complex is comprised of six invariant CD3 family chains: a CD3γ-CD3ε heterodimer, a CD3δ-CD3ε heterodimer, and a CD3ζ homodimer. Herein, we differentiate the CD3ε protomers by the CD3 component with which each pairs ($CD3\varepsilon_D$ pairs with CD3δ, and $CD3\varepsilon_G$ pairs with CD3γ) and the CD3ζ protomers as CD3ζ and CD3ζ'.

While the TCRα and TCRβ chains lack intracellular signaling domains, the CD3 proteins possess cytoplasmic immunoreceptor tyrosine activation motifs (ITAMs) that become phosphorylated upon TCR-HLA interaction and then bind and activate downstream signaling

50 kinases. Dynamic interactions between ITAMs and the membrane regulate signaling[9,10], but the
51 mechanism by which ligand binding to the extracellular TCRα-TCRβ domains results in
52 phosphorylation of cytoplasmic CD3 ITAMs remains a matter of debate. Specifically, it is unclear
53 whether ligand binding and activation involves conformational change in the TCR–CD3
54 complex. While reconstitution of TCR–CD3 signaling *in vivo* with minimal constructs has argued
55 against transmembrane conformational change[11], biochemical evidence in support of
56 conformational change[12–15] and specifically for reversible structural extension of the TCR under
57 mechanical force suggests the opposite[16], although the structural details of such conformational
58 transitions remain to be determined.

59 Structures of the hetero-octameric αβ-type TCR–CD3 have been determined by
60 cryogenic electron microscopy (cryo-EM)[5–8]. These studies revealed an antenna-like structure,
61 with the TCRα and TCRβ variable domains projecting over a ring formed by the CD3
62 ectodomains and the TCRα and TCRβ constant domains, with numerous interactions between
63 their respective transmembrane (TM) helices (Extended Data Figure 1a). Addition of HLA-
64 antigen to this complex did not meaningfully alter the conformation of the TCR–CD3[7,8], arguing
65 against models of intrinsic conformational change in the ligand-dependent TCR–CD3 activation
66 process (Extended Data Figure 1a,b).

67 However, the TCR–CD3 complexes used in these studies were solubilized in detergent.
68 Biochemical data have previously shown important roles for the lipid bilayer in the regulation of
69 TCR–CD3 signaling specifically[6,17,18], raising questions as to the physiologic relevance of the
70 determined structures. Membrane protein structure determination is generally preferable in a
71 native-like membrane environment that increases the likelihood that important protein–lipid
72 interactions are captured in the obtained molecular models[19].

73 Here, we report cryo-EM structures of a human TCR–CD3 stabilized both in detergent
74 micelles and in a native-like lipid environment. The structures reveal novel conformations for the
75 TCR–CD3 in a lipid bilayer, distinct from those previously reported, and cross-linking data
76 support the notion that these conformations represent the resting state of an unstimulated TCR–
77 CD3 on T cells. We hypothesize that the previously published structures of the TCR–CD3 in
78 detergent approximate a ligand-activated conformation and show that exit from the resting state
79 conformation is required for maximal TCR–CD3 signaling.
80

81 **Results**

82 *Structure of the NY-ESO-1-specific 1G4 TCR–CD3 in detergent micelles.* In this study, we
83 investigated the structure of the 1G4 (LY-variant) TCR–CD3. We chose the 1G4 TCR, which
84 binds to an HLA-A*02:01-restricted 9 amino acid epitope derived from the NY-ESO-1 cancer-
85 testis antigen, because it is both a model immunoreceptor and being developed as an anti-
86 cancer therapeutic[20]. To confirm that 1G4 has a similar structure to the other TCR–CD3
87 complexes analyzed in detergent, we purified this complex in glyco-diosgenin (GDN) and
88 determined its structure by cryo-EM to a nominal resolution of 3.3 Å (Figure 1a, Extended Data
89 Figure 1c-f, Extended Data Table 1, Supplementary Methods Figures 1, 2, 5-8). Herein, this
90 model and the conformation it represents will be abbreviated as “GDN.” Overall, GDN was very
91 similar to the structures of three other TCR–CD3 constructs, including those with and without
92 HLA bound (Extended Data Figure 1g). This is not surprising, given the nearly identical CD3
93 and TCR constant region sequences shared by these receptors (Extended Data Figure 1h).
94

95 *Structure of the TCR–CD3 in a native-like lipid environment.* To determine the structure of the
96 1G4 TCR–CD3 in a native-like lipid environment, we reconstituted the TCR–CD3 complex into
97 proteolipid nanodiscs loaded with mammalian polar lipids and cholesteryl hemisuccinate

98 (Supplementary Methods Figure 1). Computational processing of cryo-EM data yielded two
99 distinct maps determined to nominal resolutions of 3.3 to 3.1 Å (for locally refined maps used for
100 model building and refinement; Supplementary Methods Figures 3-5, Extended Data Figure 2).
101 We denote these as nanodisc (ND)-I and ND-II. These maps were clearly different from GDN
102 (Figure 1) and the previously published TCR structures. Attempts to bias the particle search
103 towards the published conformations with projections of the structure in detergent or that same
104 structure docked into a lipid nanodisc model did not yield any maps approximating the
105 previously published conformation (Supplementary Methods Figure 3).

106 Despite equal or higher nominal overall resolutions than GDN, ND-I and ND-II were not
107 as high quality (compare local resolution estimations in Extended Data Figure 2d,h with
108 Extended Data Figure 1f). This was likely due to a high degree of conformational variability, but
109 also due in part to map anisotropy (compare Extended Data Figure 2c,g to Extended Data
110 Figure 1e). Efforts to improve the orientation distribution of the particles with graphene oxide
111 grids and fluorinated detergents did not improve reconstruction quality (data not shown).
112 Nonetheless, these maps were of sufficient quality to build models into the density, with much of
113 the density having estimated local resolution of better than 4 Å.

114 Molecular models were built for ND-I and ND-II by docking the GDN structure into the
115 maps and refining them by standard approaches (Extended Data Table 1, Supplementary
116 Methods Figures 6-8; see Supplementary Methods for details). These models reveal two distinct
117 but related conformations of the TCR–CD3 (Figure 1a). The ND structures show two large
118 conformational changes relative to GDN: a “closure” of the TCR ectodomains against the CD3
119 ectodomains (Figure 1a,b) and a “compaction” of the juxtamembrane (JM) linker peptides
120 (Figure 1a,c,d). Collectively, these changes shorten the TCR projection into the extracellular
121 milieu by approximately 35 Å. Closure of the TCR ectodomains (Figure 1b) results in part from
122 rotation of the variable domains towards their respective constant domains about the

interdomain hinge region (Extended Data Figure 3a,b). Relative to the "extended" JM linker conformations seen in GDN, the CD3 JM linkers are compacted, with closer approximation of the CD3 ectodomains to the amino-terminal ends of their TM helices (Figure 1c,d).

The conformational changes in the TCR ectodomains are accompanied by rotations of TM helices. While the in-plane arrangement of the TM helices is largely similar when viewed along the membrane normal (Figure 1e), examination from orthogonal axes reveals differences in TM helix conformation. Compaction of the CD3 JM linkers requires opening of the angle between the TM helices of the CD3$\varepsilon\delta$ and CD3$\varepsilon\gamma$ pairs by 23° (from 31° to 54°) and 28° (from 39° to 67°), respectively, when comparing ND-II with GDN (Figure 1c,d). For ND-I, the TM helices of the CD3$\varepsilon\delta$ are bent, with the first helical turn displaying a wide splay (76°, Extended Data Figure 3c), but the overall angle between the modeled helices (46°) is intermediate to ND-II and GDN. The CD3ε_G TM helix was not modeled, as its register could not be confirmed, and thus the CD3$\varepsilon\gamma$ TM angle was not measured. Additionally, there is splaying of the TCRβ and distal CD3ζ TM helices away from the membrane normal (Figure 1f). In GDN, the TCRα TM helix extends outward past the amino-terminal ends of the CD3 TM helices, where it is ensconced by the extended CD3 JM linkers. Compaction of the JM linkers in nanodisc necessitates reorganization of the first turn of the TCRα TM helix, which is unstructured and displaced towards the lipid bilayer (Figure 1f). Taken together, these cryo-EM maps reveal marked conformational differences between the TCR–CD3 in detergent micelles and a lipid bilayer.

Additionally, the transmembrane helices of ND-I and ND-II appear shorter than in GDN. Specifically, these structures lack clear density for the cluster of basic and aromatic amino acids visualized in GDN that extend the TM helices (Extended Data Figure 3d). In a membrane, these extensions would likely be interfacial or extend into the cytoplasm[21]. Although there is additional

147 density beyond the modeled carboxy-termini of some of these shortened helices in ND-I and
148 ND-II, it is not of sufficient quality to model with confidence (Extended Data Figure 3e,f). This
149 suggests the TCR–CD3 TM helices are less rigid in the inner leaflet of a lipid bilayer than in a
150 micelle.
151
152 *Lipid interactions with the TCR–CD3.* The TCR–CD3 is known to interface directly with
153 membrane cholesterol[22], and the binding sites have been visualized in previously published
154 structures[6]. In GDN, ND-I, and ND-II, density corresponding to two cholesterols in the previously
155 published structures was again apparent (Extended Data Figure 3g). The two cholesterol
156 molecules in ND-I and ND-II are oriented tail-to-tail in a groove between CD3ζ', TCRα, TCRβ,
157 and CD3γ, as in GDN (Figure 2a). However, the compaction-associated changes in the TCR–
158 CD3 TM helices results in a sliding of the cholesterol molecules towards each other, with
159 deflection of their branched aliphatic tails to prevent clashing (Figure 2a, insets). We refer to the
160 cholesterol molecules as $Chol_A$ and $Chol_B$, corresponding to the TCR–CD3 TM helix with which
161 each is approximated. The deflected tail of $Chol_B$ is interposed between adjacent TM helices,
162 accommodated by their increased splay in the compact conformation (Figure 2b, inset). The
163 cholesterol-binding groove is more open to the membrane bilayer in nanodiscs, creating a
164 possible path for cholesterol loading into the assembled TCR–CD3 and/or exchange with the
165 membrane environment (asterisks in Figure 2b, bottom left).
166 Imaging of the TCR–CD3 in a lipid bilayer revealed additional sites of protein–lipid
167 interaction. Unmodeled tubular densities consistent with phospholipid acyl chains are present at
168 several sites adjacent to the TCR–CD3 TM helices (yellow densities, Extended Data Figure 3h-
169 k). Structured lipid is seen parallel to the tail-to-tail cholesterol dimer, filling the aforementioned
170 channel between the cholesterol-binding groove and the bulk membrane lipids (Figure 2b,

171 bottom left; Extended Data Figure 3g). Splay of the CD3ζ TM helix away from that of CD3ε_D
172 enlarges a cavity, which is filled by several presumptive lipid acyl chains in the nanodisc
173 (Extended Data Figure 3j). Additional probable sites of structured lipid include a shroud of
174 density over the CD3ζ TM helices (Extended Data Figure 3h) and in the cleft over the TCRαβ
175 TM helices between CD3δ and CD3ε_G (Extended Data Figure 3i).

176 The ND-I and ND-II maps show clear density for the proteolipid nanodisc that enshrouds
177 not only the TM helices, but also the membrane proximal faces of the TCR–CD3 ectodomains
178 (Figure 3a, left). The lipid contacts with the CD3 ectodomains are apparent even in maps
179 contoured at a higher threshold, consistent with high occupancy (Figure 3a, right). While the
180 CD3 ectodomain surfaces are generally poorly evolutionarily conserved in comparison to the
181 TM helices, patches on the membrane-proximal surfaces of the CD3 ectodomains do show high
182 sequence conservation (Figure 3a,c). These highly conserved ectodomain surface patches
183 (black triangles in Figure 3b-e) interface with the extracellular membrane leaflet and are neutral
184 to electropositive (Figure 3e), facilitating phospholipid head group interactions. Of note, we
185 observe a similar conserved electropositive patch at the interface of CD79αβ[23], the analogous
186 ITAM-bearing chains in the B-cell receptor, raising the prospect that this interface may also
187 favor membrane interactions and a different conformation in the lipid bilayer from that reported
188 in detergent micelles (Extended Data Figure 4).

189

190 *Probing TCR conformation in situ*. Which conformation of the TCR–CD3 is the physiologic
191 resting state on the cell membrane: the open/extended conformation seen in detergent micelles,
192 or the closed/compacted conformations seen in the lipid bilayer of the nanodisc? Given that the
193 lipid bilayer of a nanodisc more closely approximates the physicochemical milieu of the plasma
194 membrane, we hypothesized that the TCR–CD3 is closed and compacted in the absence of

195 activating ligand *in vivo.* To test this notion, we engineered a series of disulfide bonds that would
196 only be geometrically favorable in ND-I and/or ND-II but not GDN (or vice versa), and we read
197 out their presence or absence by one of the following approaches: (1) non-reducing sodium
198 dodecyl sulfate-polyacrylamide gel electrophoresis (SDS-PAGE) and Western blot of whole cell
199 lysates for interchain disulfides, or (2) mass spectrometry on affinity-purified protein for
200 intrachain disulfides. Analysis of disulfide bonds in the Protein Databank have shown that
201 disulfide bonds almost never have a Cys-Cys Cα-Cα distance greater than 7 Å, with most being
202 between 5 and 6.5 Å[24]. Accordingly, we sought residue pairs in the TCR–CD3 ectodomains with
203 Cα-Cα distances below 7 Å in one conformation and above 7 Å in the other as candidates for
204 disulfide engineering.

205 The interface between CD3δ and TCRα contains several pairs of residues with geometry
206 favorable for engineered disulfide formation in ND-I but not GDN (Figure 4a). As TCRα and
207 TCRβ are linked by an interchain disulfide natively (Extended Data Figure 5a), formation of a
208 TCRα–CD3δ disulfide would result in an upward gel shift of the TCRαβ heterodimer in
209 nonreducing SDS-PAGE. For all three tested engineered disulfide pairs meeting the 7 Å Cα-Cα
210 distance constraint, a gel shift consistent with TCRα–CD3δ disulfide formation was observed
211 (Figure 4b, asterisks; all full-length gels in Supplementary Methods Figure 9). Confirming that
212 this mass shift was due to disulfide formation, no gel shift was apparent under reducing
213 conditions (Supplementary Methods Figure 9b). Moreover, the mass shift was due to the
214 formation of the engineered disulfide and not an off-target bond, as adduct formation was only
215 seen when both residues in a given target pair were mutated to cysteines (Figure 4b). As an
216 internal negative control, a permutation of cysteine mutants at this interface not meeting
217 geometric criteria for disulfide formation in ND-I (TCRα S78C – CD3δ N38C, Figure 4a, right,
218 orange labels) was produced. It did not form a disulfide *in vivo* (Figure 4b, orange) despite S78C

219 and N38C successfully pairing with cognate cysteine mutants that did meet the inter-Cα
220 threshold. This control shows the structural precision and specificity of the engineered disulfide
221 bond approach. These experiments were performed using whole-cell lysates, but we obtained
222 similar results with NiNTA-affinity-purified protein (Extended Data Figure 5b), and we were able
223 to reconstitute the two G79C-crosslinked mutants into nanodiscs (Extended Data Figure 5c,d),
224 suggesting proper folding and assembly of the holo TCR–CD3.

225 The region around the TCRα and TCRβ interdomain hinges is also notably different in
226 the closed/compacted conformation compared to the open/extended one, with the variable
227 domains coming into closer apposition with their respective constant domains, allowing the
228 engineering of conformation-specific disulfide pairs in this region (Figure 4c,d). We probed
229 formation of these intrachain disulfides by mass spectrometry. Proteolytic digestion of the TCR–
230 CD3 with trypsin and chymotrypsin yielded distinct peptides, several of which were linked by
231 disulfide-bonds. Electron-transfer/higher-energy collision dissociation (EThcD) fragmentation
232 was used to fragment the disulfide-bonded peptides providing *in vacuo* reduction to the linear
233 peptide constituents along with peptide backbone fragmentation, thereby allowing unambiguous
234 identification of the engineered disulfides[25]. All native TCR–CD3 disulfides spanning two
235 proteolytic fragments (Extended Data Figure 5a) were observed in the wild-type 1G4 TCR–CD3
236 by this approach (Extended Data Table 2). For both ND conformation-compatible engineered
237 disulfides tested (Figure 4c,d), we observed formation of the engineered disulfide (Figure 4e,f
238 and Extended Data Table 2). In contrast, an engineered disulfide that would only be present in
239 the open/extended conformation (Extended Data Figure 5e) did not form *in vivo* (Extended Data
240 Table 2). Taken together, these data support the conclusion that a TCR–CD3 in the unliganded,
241 resting state adopts the closed/compact conformation *in vivo*.
242

243 *Conformational variability of the TCR–CD3 in a lipid bilayer*. To allow direct comparison of the
244 two distinct, but related, closed/compacted structures (ND-I and ND-II), they were aligned by
245 their TCRα TM helices. TCRα was chosen because it is relatively perpendicular to the
246 membrane plane (alongside CD3ζ') and thus might be least affected by any differences in TM
247 helix splay. Indeed, this alignment strategy brought the nanodisc density of their maps into
248 alignment as well (Extended Data Figure 6a), giving both models the same orientation relative
249 to the membrane bilayer. In contrast to the strong overall alignment of the TCR–CD3 TM helices
250 by this approach (Extended Data Figure 6b,c), the ectodomains of ND-I and ND-II has marked
251 conformational differences, as seen in the aligned cryo-EM densities (Extended Data Figure
252 6a,b) and the resulting protein models (Figure 5a). Comparison of the structures reveals the
253 motions allowing exchange between these conformations (Figure 5b,c, Supplementary Movie
254 1). ND-I is the most closed of the three structures in this study, and transition to ND-II requires
255 several motions: the depression of the CD3ε_D (Figure 5b) and CD3γ ectodomains (Figure 5c)
256 away from the TCR variable domains and towards the bilayer outer leaflet; rotation of the of the
257 TCRα variable domain about the interdomain hinge (Figure 5b); and retraction of the TCRβ
258 variable domain (Figure 5c). This is accompanied by sliding of CD3ζ along its helical axis
259 towards the ectodomains (Figure 5b). While the TCRα and CD3ζ' TM helices remain relatively
260 fixed in this frame of reference, the TCRβ and CD3γ TM helices shift away from the cholesterol-
261 binding groove (Figure 5d, Extended Data Figure 6c). To accommodate this movement, there is
262 rotation of $Chol_A$ and elevation of $Chol_B$ (Figure 5d), showing cholesterol to be an integral and
263 dynamic component of the TCR–CD3 structure.

264 The GDN map displays densities for many of the known asparagine (N)-linked glycans in
265 the TCR–CD3 (Extended Data Figure 6d). There were fewer densities modellable as N-linked
266 glycans in the ND-I and ND-II maps (Extended Data Figure 6d). However, all three maps show

267 an array of densities lateral to the CD3δ and TCRα ectodomains, corresponding to sites of
268 known N-linked glycosylation. In ND-II, the TCRα (linkage unclear) and CD3δ N74-linked
269 glycans are visible, emerging radially from the TCR–CD3, as in GDN, but are not well structured
270 (Figure 5e). By comparison, ND-I reveals clear reorganization of the glycans (Figure 5e), with
271 increased stacking of adjacent glycans brought into close proximity by tight ectodomain closure.
272 This arraying of N-linked glycans is reminiscent of that seen on HIV Env, where interacting
273 adjacent glycans form a structured arcade of glycan cores (Extended Data Figure 6e). Two
274 densities in the array are attributable to CD3δ N74- and TCRα N82-linked glycans, with a third
275 density emerging between them without definitive attribution (purple question mark in Figure 5e,
276 right inset). In GDN, as in other structures of TCR–CD3 in detergent, the CD3δ N38-linked
277 glycan is oriented inward towards the cleft between the TCR and CD3 ectodomains (Figure 5f,
278 top). In ND-II, CD3δ N38 is unstructured (Figure 5f, middle), but is grossly positioned at the
279 entrance to the cleft, and the linked glycan could conceivably orient either into or away from the
280 cleft. In ND-I, CD3δ N38 is structured (Figure 5f, bottom), but its glycan cannot be confidently
281 modeled. However, density protrudes from N38 into the open cleft (Figure 5f, asterisk) and
282 additional unmodeled density is seen within the cleft, consistent with the glycan remaining within
283 the cleft in the ND-I conformation.

284 The structure of the TCR variable domains in GDN is grossly unchanged from that seen
285 in previous crystal structures of the 1G4 TCR bound to HLA-β2M-antigen[26] (herein, TCR-HLA;
286 Extended Data Figure 6g). Despite the unstructuring of their amino-termini and some surface
287 loops in the ND-I and ND-II, as well as the domain-scale movements described above, there
288 was little change in the orientations of the TCR variable domains relative to one another when
289 compared to GDN and the TCR-HLA crystal structure (Extended Data Figure 6g). However,
290 differences in ectodomain closure seen between ND-I and ND-II could have consequences for

291 the accessibility of the TCR variable domains to HLA-antigen complexes. To assess the impact
292 of ectodomain cleft opening and closure on TCR–HLA interactions, we modeled the binding
293 geometry of HLA onto GDN, ND-I, and ND-II by alignment of the TCR-HLA crystal structure to
294 the TCR variable domains in our models (Figure 5g). There appears to be adequate clearance
295 for the TCR variable domains to interact with HLA in GDN and ND-II. For ND-I, the modeled fit
296 is tighter, with the CD3ε_D ectodomain predicted to be in close contact with HLA. However, on
297 assessment of space-filling model cross-sections, no overt steric clashes are evident (Figure
298 5h). Because a portion of a potentially clashing surface loop in the CD3ε_D ectodomain is not
299 modeled in ND-I, the TCR-aligned HLA model was docked into the ND-I cryo-EM density
300 (Figure 5i), but no unmodeled density appears to clash with HLA. The CD3ε_D ectodomain from
301 GDN is completely modeled and aligns closely with that from ND-I (Extended Data Figure 6f,
302 inset). As an additional sensitivity analysis, the GDN CD3ε_D ectodomain was modeled into ND-I
303 and the HLA interaction again assessed. While there is a small overlap in their space-filling
304 models (Extended Data Figure 6f), no large clashes are observed. Thus, while it remains
305 unclear what quantitative effect ectodomain cleft closure might have on HLA affinity, particularly
306 in the physiologic context of a glycosylated HLA molecule, it is at least plausible that both ND-I
307 and ND-II may be receptive to HLA binding.
308
309 *A model for TCR–CD3 conformational change in receptor activation.* Taking the above
310 structural, biochemical, and modeling data together and in context with the literature, we
311 developed a model for ligand-dependent activation of the TCR–CD3. Our data support a model
312 in which the unliganded “resting” TCR–CD3 explores a thermally accessible spectrum of
313 closed/compacted conformations from the most closed ND-I to the more open ND-II. Previous
314 data have shown HLA monomer binding to the TCR is insufficient to drive T-cell activation, but

315 that subsequent force application induces activation[27]. Force-dependent activation was
316 accompanied by an increase in TCR length normal to the membrane[16], raising the possibility
317 that the open/extended structure of the TCR reported in detergent micelles is actually an
318 approximation of a physiologically active state. We do note that other data support the
319 possibility of TCR–CD3 conformational change upon ligand binding, even without external force
320 application, suggesting an allosteric mechanism[12,28], which would also be consistent this model.
321 Moreover, TCR–CD3 opening and/or extension may be necessary for coreceptor interaction
322 with HLA bound to the TCR–CD3. Modeling the HLA class II-CD4 complex onto GDN, ND-I, and
323 ND-II reveals an unfavorable geometry for CD4 interaction with a class II HLA when bound to a
324 TCR–CD3 in the ND-I or ND-II conformation because of their proximity to the membrane
325 (Extended Data Figure 6h), at least for the CD4 conformation reported in the CD4-HLA-TCR
326 ectodomains ternary complex crystal structure[29]. In contrast, CD4-HLA can be accommodated
327 in the GDN conformation (Extended Data Figure 6h). The full ectodomain structure of the CD8
328 coreceptor has not been described, precluding a similar analysis applicable to TCRs
329 recognizing HLA class I-restricted epitopes, like the one used in this study.

330 We hypothesize that binding of HLA-antigen to the TCR–CD3 results in a structural
331 transition from the closed/compacted resting conformation to an open/extended active
332 conformation (Figure 6a). We favor this transition occurring via the ND-II conformation, which is
333 more open than ND-I and thus closer to the active state along this trajectory. Morphing the
334 closed/compacted conformation to the open/extended one (Supplementary Movie 2) highlights
335 the straightening of the TM helices towards the membrane normal (that is, decreased splay,
336 Figure 6b). These changes in TM conformation add to the plausibility of the model, as they
337 provide a means to transmit conformational changes in the ectodomains to the cytoplasmic
338 ITAMs.

339 Thus, transition from the closed/compacted to the open/extended conformation would
340 seem to require further ectodomain opening from the ND-II state (Figure 6a). We hypothesized
341 that the intra-TCRα disulfide-forming double mutant S104C–V182C (characterized above,
342 Figure 4c) would prevent ectodomain opening to the more open active conformation, and thus
343 impair ligand-dependent TCR–CD3 activation. To investigate the impact of restrained TCR–CD3
344 opening on ligand-dependent activation of T cells, we introduced wild-type and TCRα S104C–
345 V182C mutant TCR constructs into TCRαβ-negative Jurkat T cells bearing an NFAT-responsive
346 fluorescent reporter. TCR–CD3 assembly and surface localization (as assessed by anti-CD3ε
347 antibody binding) and HLA-binding competence were confirmed by flow cytometry for the
348 mutant and were comparable to cells transduced with wild-type 1G4 (Figure 6c). In the absence
349 of HLA-antigen tetramers, there was no detectable reporter fluorescence in these cells, but
350 upon exposure to HLA-antigen tetramers, cells expressing wild-type TCR–CD3 became
351 activated, with reporter fluorescence peaking 16 h after HLA-tetramer addition (Figure 6d). By
352 contrast, peak reporter fluorescence was significantly decreased in the TCRα S104C–V182C
353 mutant, with peak activation attenuated by 26% ($P < 0.05$, Figure 6d, source data in
354 Supplementary File 1) relative to wild-type on exposure to 8 μg/mL of tetramers. The TCRα
355 S104C–V182C mutant and wild-type controls were equally responsive to phorbol 12-myristate
356 13-acetate (PMA) and ionomycin, which bypass TCR–CD3 signaling to activate T cells.
357

358 **Discussion**

359 Here, we report structures of a human TCR–CD3 both in a lipid bilayer and in detergent
360 micelles. We find that the TCR–CD3 hetero-octamer assumes a spectrum of more closed and
361 compacted conformations when embedded in a lipid bilayer relative to that seen in detergent
362 micelles, that the closed/compacted conformation is indeed the native unliganded state of the

363 TCR–CD3, and that exit from this conformation by ectodomain opening is necessary for
364 maximal ligand-dependent activation of the TCR–CD3. While this latter finding does not rule out
365 roles for TCR–CD3-extrinsic phenomena (e.g., higher-order clustering, steric exclusion of
366 inhibitory phosphatases) in the activation of the TCR–CD3 or regulation thereof, it argues that
367 intrinsic conformational change in the TCR–CD3 is necessary for early TCR–CD3 activation and
368 argues against previous models that have excluded this requirement[11,30].

369 Broadly, these findings reinforce the importance of structural interrogation of membrane
370 proteins in lipid environments that closely resemble their physiologic environment. Comparison
371 of TCR–CD3s in detergent micelles in the absence and presence of activating ligand had
372 revealed no change in TCR–CD3 structure[7,8], consistent with models excluding TCR–CD3
373 conformational change in the activation process. Although these studies were technically well
374 performed, our results now reveal that they did not identify the true resting state of the TCR–
375 CD3, calling into question the conclusion that there is no intrinsic conformational change in the
376 TCR–CD3 during ligand-dependent activation.

377 Additionally, the structures in detergent did not capture the full scope of TCR–CD3
378 interaction with the membrane. Not only are membrane lipids closely interwoven with the TM
379 helices, but large conserved surface patches on the ectodomains mediate lipid–protein
380 interactions, likely partially counteracting the thermodynamic costs of JM linker compaction and
381 “spring loading” the TCR with potential energy for conformational change during activation. In
382 this model, ligand binding and/or force application provides the activation energy to release the
383 membrane-binding surfaces of the CD3 ectodomains and allow JM extension. This would be
384 consistent with existing models of TCR–CD3 response to force, which invoke conformational
385 changes with free energy barriers rendering them inaccessible to thermal motion alone[31].
386 Detergent extraction would overcome this thermodynamic barrier by removing the lipid bilayer
387 all together. During reconstitution into nanodiscs, we first extracted the TCR–CD3 complex in

388 detergent, opening and extending the receptor, which suggests that the addition of a lipid bilayer
389 is sufficient to reset the TCR–CD3 to its resting conformation without the need for extrinsic
390 chaperones. Lastly, we note that a similar conserved surface patch is present on the CD79
391 heterodimer in the B-cell receptor[23], raising the possibility that other hetero-multimeric ITAM-
392 containing immunoreceptors exploit protein surface interactions with the lipid bilayer to constrain
393 conformation.

394 As with the TCR–CD3 structures in detergent, the CD3 ITAMs are not visible in our
395 structures. The ITAMs are membrane-associated in the unliganded state[9,10], but are likely to be
396 radially disordered along the intracellular membrane face. However, the TM helix movements
397 seen between our closed/compacted and the open/extended conformations suggest a means
398 for communication of extracellular conformational changes in the TCR–CD3 complex to the
399 ITAMs. Within the cytoplasmic domains of CD3 proteins, the basic residues proximal to the CD3
400 TM helix are critical for ITAM association with the membrane[9,10]. Upon transition from the
401 receptive to the hypothesized active conformation, the decreased splay in the CD3 TM helices
402 could alter basic patch interaction with the membrane and favor ITAM release.

403 Analysis of the basal conformational heterogeneity of the TCR–CD3 suggests novel
404 means of TCR–CD3 regulation. The TCRα and CD3δ glycan ordering observed in the ND-I
405 conformation is notably different from the glycan arrangement in the more open ND-II
406 conformation or the TCR–CD3 in detergent. While molecular modeling of the branched glycan
407 sugars was not possible with sufficient confidence, the stacked arrangement of glycan core
408 densities raises the possibility of extensive hydrogen bonding between the glycan branches
409 distally and perhaps also with TCR–CD3 surface residues. While glycan–glycan and glycan–
410 protein interactions are well described *in trans*, there are fewer examples of structured glycan–
411 glycan interactions within a given protein or stable complex. The human immunodeficiency
412 virus-1 Env protein is an example of the latter[32,33] and the arrangement of the radial glycan array

413 in ND-I is reminiscent of that seen in crystallographic studies of Env. However, the stacking of
414 glycans observed in the TCR–CD3 is unique in being protein conformation-dependent. Breaking
415 an extensive glycan hydrogen-bonding network to transition out of ND-I would be energetically
416 costly, and thus modification of TCR–CD3 glycosylation could serve as a means of
417 posttranslational regulation of the TCR–CD3 activation threshold by increasing or decreasing
418 the free energy barrier to ND-I exit.

419 Previous studies have explored the role of cholesterol in the regulation of TCR–CD3
420 activation[6,18,22]. The substantive movements of the two cholesterol molecules seen between
421 TCR–CD3 conformations raise the possibility that changes in the sterol composition of the T-cell
422 membrane (either global or local) could alter TCR–CD3 activity even prior to ligand binding by
423 shaping the basal TCR–CD3 conformational landscape. Moreover, our structures reveal
424 channels for cholesterol loading or exchange with the lipid bilayer not previously observed,
425 making it plausible that already assembled TCR–CD3 could respond to changes in membrane
426 sterol content. Non-sterol lipid species are also known regulators of T-cell signaling[17], including
427 phosphoinositol lipids[34,35] and oxidized lipids in the tumor microenvironment[36]. This work
428 delineates multiple sites of structured interaction between the TCR–CD3 and membrane lipids
429 beyond the sterol-binding site, which may allow specific lipids to modulate TCR–CD3
430 conformation and activity.

431 The extensive contacts between TCR variable domain residues and those of the TCR
432 constant domains or CD3 ectodomains in the closed/compacted conformations raises questions
433 about how variation at these sites might confer specific baseline sensitivities to given TCR
434 alleles. Whether use of certain V or J alleles changes the occupancy of different segments of
435 the TCR–CD3 conformational landscape will need to be determined and has broad implications
436 for vaccine design and immunotherapy engineering. Likewise, whether individually rare germline
437 coding variants in the TCR constant domain *loci* or CD3 proteins affects an individual's basal T-

438 cell reactivity is unclear outside of known deleterious loss-of-function alleles[37]. Such information
439 might predict individual propensity for autoimmunity or responsiveness to immune-oncology
440 agents and will provide insights for engineering TCRs with favorable activity profiles[38].
441
442 **Methods**
443 Full methods are detailed in the Supplementary Methods.
444
445 **Data Availability Statement**
446 Cryo-EM maps and atomic coordinates for GDN, ND-I, and ND-II have been deposited in the
447 Protein Data Bank and Electron Microscopy Data Bank with the following accession numbers:
448 GDN, PDB 9BBC, EMD-44417; ND-I, PDB 8TW4, EMD-41658; ND-II, PDB 8TW6, EMD-41660.
449
450 **Acknowledgements**
451 The authors thank the members of the Walz, T. de Lange (RU), and R. K. Hite (MSKCC) labs
452 and Drs. E. L. Reinherz (HMS, DFCI) and W. D. Tap (MSKCC) for insightful conversations. We
453 thank M. Ebrahim, J. Sotiris, and H. Ng at the Evelyn Gruss Lipper Cryo-EM Resource Center of
454 The Rockefeller University for assistance with cryo-EM data collection. We thank Pujita Das for
455 excellent technical assistance. R.Q.N. was supported by National Institutes of Health (NIH)
456 grants T32CA9207, KL2TR001865, and UL1TR001866; the Black Family Metastasis Center at
457 Rockefeller University; the Shapiro-Silverberg Fund for the Advancement of Translational
458 Research; and the Mark Foundation for Cancer Research (R.Q.N. and T.W.). C.A.K. was
459 supported, in part, by NIH grants R37 CA259177, R01 CA269733, R01 CA286507, P30
460 CA008748, and P50 CA217694; Cycle for Survival and the Shteinbuk and Mead Family; the
461 Parker Institute for Cancer Immunotherapy; and The Sarcoma Center at MSKCC. Mass
462 spectrometry data was generated by the Proteomics Resource Center at The Rockefeller

463 University (RRID:SCR_017797) using instrumentation funded by the Sohn Conferences
464 Foundation and the Leona M. and Harry B. Helmsley Charitable Trust.

465

466 **Author Contributions**

467 R.Q.N conceived of the project, designed and performed experiments, analyzed data, built
468 models, and wrote and revised the manuscript; F.Y. designed and performed experiments and
469 analyzed data; S.H. designed and performed experiments and analyzed data; M.B. performed
470 experiments and analyzed data; H.M. designed and performed experiments and analyzed data;
471 C.A.K. designed experiments, analyzed data, and revised the manuscript; T.W. designed
472 experiments, analyzed data, and revised the manuscript.

473

474 **Competing Interests**

475 C.A.K. is an inventor on patents related to TCR discovery and public neoantigen-specific TCRs
476 and is recipient of licensing revenue shared according to MSKCC institutional policies. C.A.K.
477 has consulted for or is on the scientific advisory boards for Achilles Therapeutics, Affini-T
478 Therapeutics, Aleta BioTherapeutics, Bellicum Pharmaceuticals, Bristol Myers Squibb,
479 Catamaran Bio, Cell Design Labs, Decheng Capital, G1 Therapeutics, Klus Pharma, Obsidian
480 Therapeutics, PACT Pharma, Roche/Genentech, Royalty Pharma, and T-knife. C.A.K. is a
481 scientific co-founder and equity holder in Affini-T Therapeutics.

482

483 **References**

484 1. Janeway, C. A. *et al. Immunobiology*. (Garland Science, 2001).
485 2. Reinherz, E. L. The structure of a T-cell mechanosensor. *Nature* **573**, 502–504 (2019).
486 3. Courtney, A. H., Lo, W.-L. & Weiss, A. TCR Signaling: Mechanisms of Initiation and
487 Propagation. *Trends Biochem. Sci.* **43**, 108–123 (2018).

488 4. Mariuzza, R. A., Agnihotri, P. & Orban, J. The structural basis of T-cell receptor (TCR)
489 activation: An enduring enigma. *J. Biol. Chem.* **295**, 914–925 (2020).
490 5. Dong, D. *et al.* Structural basis of assembly of the human T cell receptor–CD3 complex.
491 *Nature* **573**, 546–552 (2019).
492 6. Chen, Y. *et al.* Cholesterol inhibits TCR signaling by directly restricting TCR–CD3 core tunnel
493 motility. *Mol. Cell* **82**, 1278-1287.e5 (2022).
494 7. Sušac, L. *et al.* Structure of a fully assembled tumor-specific T cell receptor ligated by pMHC.
495 *Cell* **185**, 3201-3213.e19 (2022).
496 8. Saotome, K. *et al.* Structural analysis of cancer-relevant TCR–CD3 and peptide-MHC
497 complexes by cryoEM. *Nat. Commun.* **14**, 2401 (2023).
498 9. Xu, C. *et al.* Regulation of T Cell Receptor Activation by Dynamic Membrane Binding of the
499 CD3ε Cytoplasmic Tyrosine-Based Motif. *Cell* **135**, 702–713 (2008).
500 10. Zhang, H., Cordoba, S.-P., Dushek, O. & Anton van der Merwe, P. Basic residues in the
501 T-cell receptor ζ cytoplasmic domain mediate membrane association and modulate signaling.
502 *Proc. Natl. Acad. Sci.* **108**, 19323–19328 (2011).
503 11. James, J. R. & Vale, R. D. Biophysical Mechanism of T Cell Receptor Triggering in a
504 Reconstituted System. *Nature* **487**, 64–69 (2012).
505 12. Minguet, S., Swamy, M., Alarcón, B., Luescher, I. F. & Schamel, W. W. A. Full activation
506 of the T cell receptor requires both clustering and conformational changes at CD3. *Immunity*
507 **26**, 43–54 (2007).
508 13. Gil, D., Schamel, W. W. A., Montoya, M., Sánchez-Madrid, F. & Alarcón, B. Recruitment
509 of Nck by CD3 epsilon reveals a ligand-induced conformational change essential for T cell
510 receptor signaling and synapse formation. *Cell* **109**, 901–912 (2002).
511 14. Natarajan, K. *et al.* An allosteric site in the T-cell receptor Cβ domain plays a critical
512 signalling role. *Nat. Commun.* **8**, 15260 (2017).

513 15. Rangarajan, S. *et al.* Peptide-MHC (pMHC) binding to a human antiviral T cell receptor
514 induces long-range allosteric communication between pMHC- and CD3-binding sites. *J. Biol.*
515 *Chem.* **293**, 15991–16005 (2018).
516 16. Das, D. K. *et al.* Force-dependent transition in the T-cell receptor β-subunit allosterically
517 regulates peptide discrimination and pMHC bond lifetime. *Proc. Natl. Acad. Sci.* **112**, 1517–
518 1522 (2015).
519 17. Wu, W., Shi, X. & Xu, C. Regulation of T cell signalling by membrane lipids. *Nat. Rev.*
520 *Immunol.* **16**, 690–701 (2016).
521 18. Wang, F., Beck-García, K., Zorzin, C., Schamel, W. W. A. & Davis, M. M. Inhibition of T
522 cell receptor signaling by cholesterol sulfate, a naturally occurring derivative of membrane
523 cholesterol. *Nat. Immunol.* **17**, 844–850 (2016).
524 19. Notti, R. Q. & Walz, T. Native-like environments afford novel mechanistic insights into
525 membrane proteins. *Trends Biochem. Sci.* (2022).
526 20. Robbins, P. F. *et al.* A Pilot Trial Using Lymphocytes Genetically Engineered with an NY-
527 ESO-1–Reactive T-cell Receptor: Long-term Follow-up and Correlates with Response. *Clin.*
528 *Cancer Res.* **21**, 1019–1027 (2015).
529 21. Ulmschneider, M. B. & Sansom, M. S. P. Amino acid distributions in integral membrane
530 protein structures. *Biochim. Biophys. Acta BBA - Biomembr.* **1512**, 1–14 (2001).
531 22. Swamy, M. *et al.* A Cholesterol-Based Allostery Model of T Cell Receptor
532 Phosphorylation. *Immunity* **44**, 1091–1101 (2016).
533 23. Su, Q. *et al.* Cryo-EM structure of the human IgM B cell receptor. *Science* **377**, 875–880
534 (2022).
535 24. Gao, X., Dong, X., Li, X., Liu, Z. & Liu, H. Prediction of disulfide bond engineering sites
536 using a machine learning method. *Sci. Rep.* **10**, 10330 (2020).

537 25. Liu, F., van Breukelen, B. & Heck, A. J. R. Facilitating Protein Disulfide Mapping by a
538 Combination of Pepsin Digestion, Electron Transfer Higher Energy Dissociation (EThcD), and
539 a Dedicated Search Algorithm SlinkS*. *Mol. Cell. Proteomics* **13**, 2776–2786 (2014).
540 26. Chen, J.-L. *et al.* Structural and kinetic basis for heightened immunogenicity of T cell
541 vaccines. *J. Exp. Med.* **201**, 1243–1255 (2005).
542 27. Kim, S. T. *et al.* The αβ T Cell Receptor Is an Anisotropic Mechanosensor *. *J. Biol.*
543 *Chem.* **284**, 31028–31037 (2009).
544 28. Lanz, A.-L. *et al.* Allosteric activation of T cell antigen receptor signaling by quaternary
545 structure relaxation. *Cell Rep.* **36**, 109375 (2021).
546 29. Yin, Y., Wang, X. X. & Mariuzza, R. A. Crystal structure of a complete ternary complex of
547 T-cell receptor, peptide-MHC, and CD4. *Proc. Natl. Acad. Sci. U. S. A.* **109**, 5405–5410
548 (2012).
549 30. Fernandes, R. A. *et al.* T Cell Receptors are Structures Capable of Initiating Signaling in
550 the Absence of Large Conformational Rearrangements*. *J. Biol. Chem.* **287**, 13324–13335
551 (2012).
552 31. Reinherz, E. L., Hwang, W. & Lang, M. J. Harnessing αβ T cell receptor mechanobiology
553 to achieve the promise of immuno-oncology. *Proc. Natl. Acad. Sci.* **120**, e2215694120
554 (2023).
555 32. Stewart-Jones, G. B. E. *et al.* Trimeric HIV-1-Env Structures Define Glycan Shields from
556 Clades A, B, and G. *Cell* **165**, 813–826 (2016).
557 33. Lee, J. H., de Val, N., Lyumkis, D. & Ward, A. B. Model Building and Refinement of a
558 Natively Glycosylated HIV-1 Env Protein by High-Resolution Cryoelectron Microscopy.
559 *Structure* **23**, 1943–1951 (2015).
560 34. Chouaki Benmansour, N. *et al.* Phosphoinositides regulate the TCR/CD3 complex
561 membrane dynamics and activation. *Sci. Rep.* **8**, 4966 (2018).

562 35. Costello, P. S., Gallagher, M. & Cantrell, D. A. Sustained and dynamic inositol lipid
563 metabolism inside and outside the immunological synapse. *Nat. Immunol.* **3**, 1082–1089
564 (2002).
565 36. Xu, S. *et al.* Uptake of oxidized lipids by the scavenger receptor CD36 promotes lipid
566 peroxidation and dysfunction in CD8+ T cells in tumors. *Immunity* **54**, 1561-1577.e7 (2021).
567 37. Kent, A., Longino, N. V., Christians, A. & Davila, E. Naturally Occurring Genetic
568 Alterations in Proximal TCR Signaling and Implications for Cancer Immunotherapy. *Front.*
569 *Immunol.* **12**, (2021).
570 38. Klebanoff, C. A., Chandran, S. S., Baker, B. M., Quezada, S. A. & Ribas, A. T cell
571 receptor therapeutics: immunological targeting of the intracellular cancer proteome. *Nat. Rev.*
572 *Drug Discov.* **22**, 996–1017 (2023).
573
574

575 **Figures and Legends**

576 **Figure 1**

577

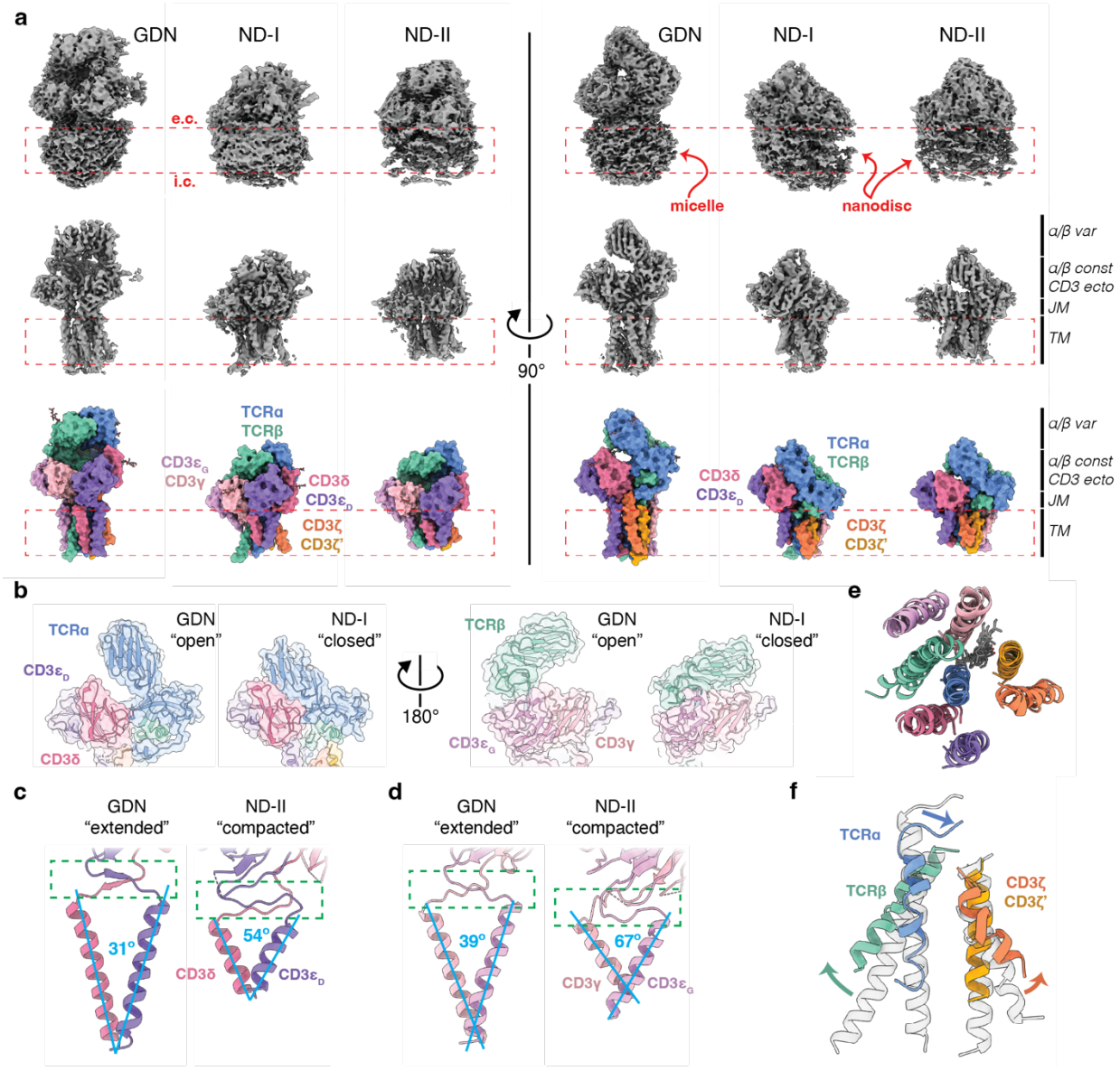

578

579

580 **Figure 1: Architecture of the TCR–CD3 in a native-like lipid environment.** (a) Cryo-EM
581 maps (top, middle) and space-filling solvent-excluded surfaces for the models (bottom; herein,
582 model surfaces) of the TCR–CD3 in a detergent micelle (GDN) and in nanodiscs (conformations
583 ND-I and ND-II). Top row shows cryo-EM density (without local refinement) after B-factor
584 sharpening, contoured to a low threshold to highlight micelle and nanodisc positioning. Red
585 dashed box indicates approximate plasma membrane span as inferred from the micelle and
586 nanodisc densities (red arrows and labels). Extracellular and intracellular faces indicated as e.c.
587 and i.c., respectively. Middle row shows DeepEMhancer-sharpened maps after local refinement,
588 accentuating the protein and glycan densities. Protein regions indicated at far right abbreviated
589 as follows: var, variable domains; ecto, ectodomains; const, constant domains; JM,
590 juxtamembrane linkers; TM, transmembrane helices. (b) Comparison of GDN and ND-I models,
591 highlighting ectodomain closure in the context of a lipid bilayer. Model backbone cartoon inside
592 transparent model surfaces shown. (c,d) Comparison of GDN and ND-II models, highlighting
593 juxtamembrane linker compaction in the direction normal to the lipid bilayer (green dashed box)
594 and coincident splay of the TM helices (cyan lines and angular measures). The CD3εδ and
595 CD3εγ heterodimers are shown in (c) and (d), respectively. (e) Overlay of the TM helices in the
596 detergent micelle and lipid bilayer (both ND-I and ND-II), viewed from the extracellular space
597 showing similar overall arrangement. (f) Comparison of GDN (transparent grey) and ND-II (solid,
598 color-coded) transmembrane helices aligned to TCRα residues 245-260 and viewed parallel to
599 the plasma membrane. Green and orange arrows highlight increased splay of the TCRβ
600 transmembrane helix and the carboxy-terminal end of the CD3ζ TM helix, respectively. Blue
601 arrow highlights the unstructuring and deflection of the first helical turn at the amino-terminus of
602 the TCRα transmembrane helix in the lipid bilayer.
603

604 **Figure 2**

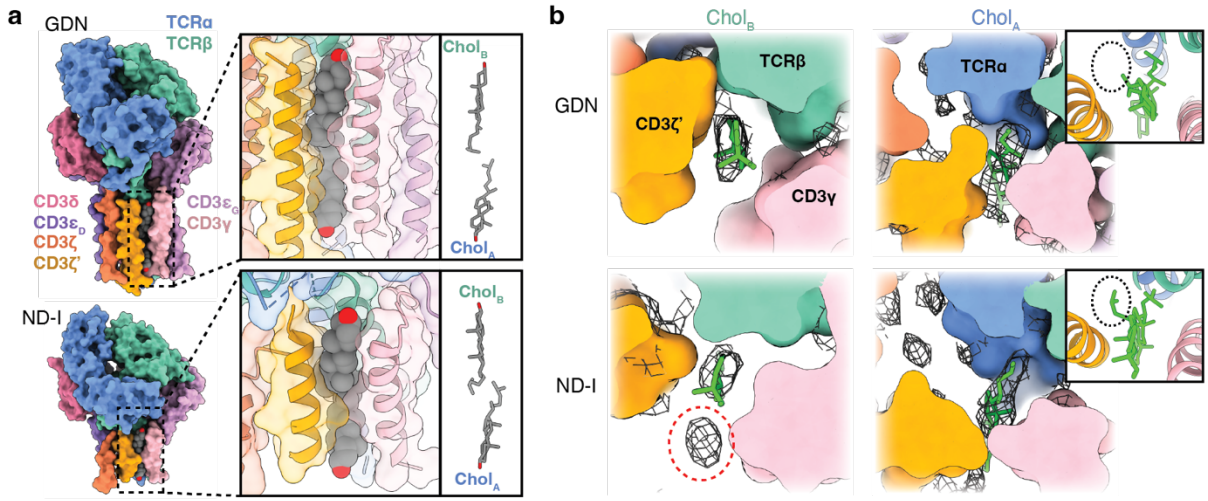

605
606
607

608 **Figure 2: TCR–CD3–lipid interactions.** (a) Comparison of the cholesterol-binding sites of the
609 TCR in detergent (top) and in nanodiscs (bottom). Overview shown at left and insets show the
610 cholesterol-binding sites in detail (left) and with protein removed (right) to highlight the deflection
611 of the branched aliphatic tails. $Chol_B$ denotes the cholesterol proximal to the ectodomains and
612 the TCRβ transmembrane helix; $Chol_A$ denotes the cholesterol proximal to the cytoplasmic face
613 and the TCRα transmembrane helix. (b) Sections parallel to the membrane plane highlighting
614 the opening of the cholesterol-binding groove to the lipid environment in nanodiscs relative to
615 that in detergent. Sections are shown at the levels of $Chol_A$ and $Chol_B$, as indicated. Density
616 from locally refined and B-factor-sharpened cryo-EM maps is shown as black mesh,
617 cholesterols in lime green. Dashed circle highlights structured lipid density in the nanodisc
618 bilayer adjacent to the opened cholesterol-binding groove. Insets show the cholesterol binding
619 groove from the same angle as the main panels, but with both cholesterols shown in the slice,
620 highlighting intercalation of the deflected $Chol_B$ aliphatic chain between TM helices in nanodiscs
621 (black dashed oval) as compared to the structure in GDN.
622
623

Figure 3

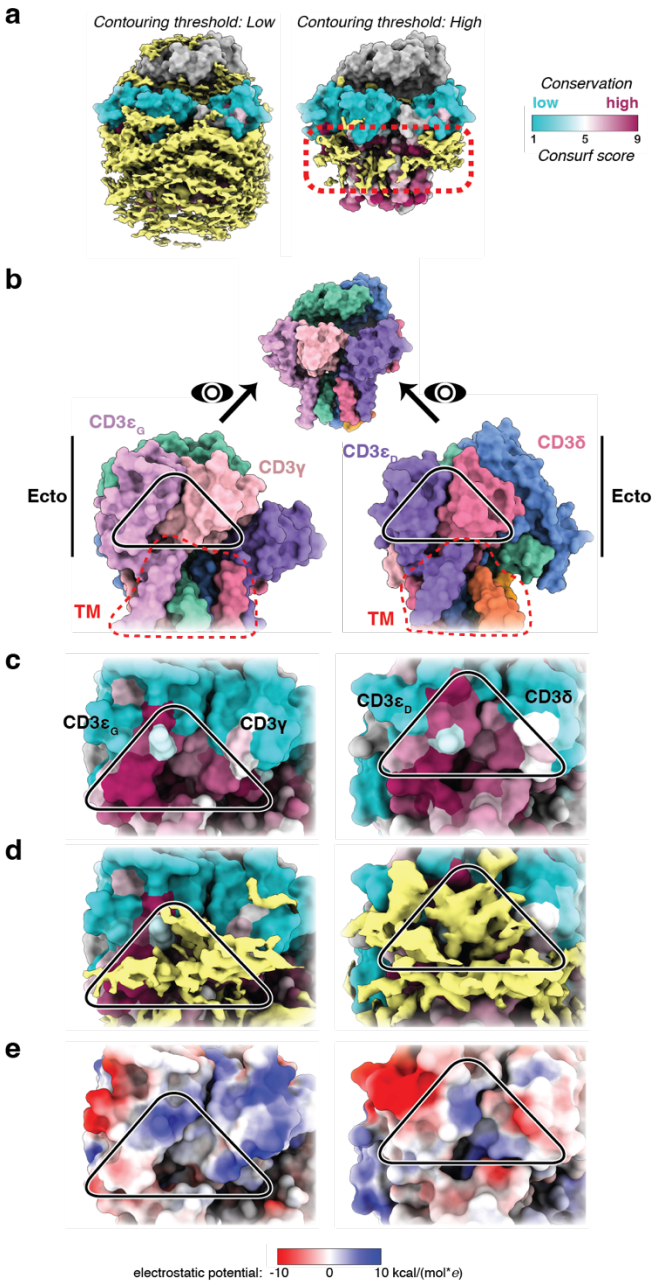
a
Contouring threshold: Low
Contouring threshold: High
Conservation
low
high
1
5
9
Consurf score
b
CD3εG
CD3γ
Ecto
TM
CD3εD
CD3δ
Ecto
TM
c
CD3εG
CD3γ
CD3εD
CD3δ
d
e
electrostatic potential: -10
0
10 kcal/(mol*e)

Figure 3: Conserved CD3 surface patches form extensive membrane contacts. (a) ND-II model surface colored by sequence conservation (Consurf score 1 through 9) and yellow unmodeled map density from the nanodisc enshrouding the TCR–CD3 TM helices and membrane-proximal ectodomain surfaces. When visualized with a higher contouring threshold (right), structured lipid density adjacent to the CD3 ectodomains persisted (red dotted box). Note also the relative sequence conservation in the CD3 TM helices and membrane-adjacent ectodomain surfaces, but not solvent-exposed surfaces. (b) Top, ND-II space-filling model for orientation. Arrows and eyes indicate the viewing direction for inspection of the CD3εγ and CD3εδ interfaces examined in the lower panels. Bottom, overviews orienting the close-up views in panels c through e. Red dashed lines denote the border between TM and ectodomain (Ecto) surfaces. (c) Close-up views of the membrane-proximal face of the CD3 heterodimers, with black triangles highlighting the conserved surface patch at the subunit interface. (d) Lipid density (yellow) is most robust over this conserved patch, visualized at high contouring threshold (as in panel a, right). (e) The conserved ectodomain patch is relatively electropositive compared to the surrounding ectodomain surfaces colored by electrostatic potential (red to blue, -10 to 10 kcal/(mol*e)).

647 **Figure 4**

648

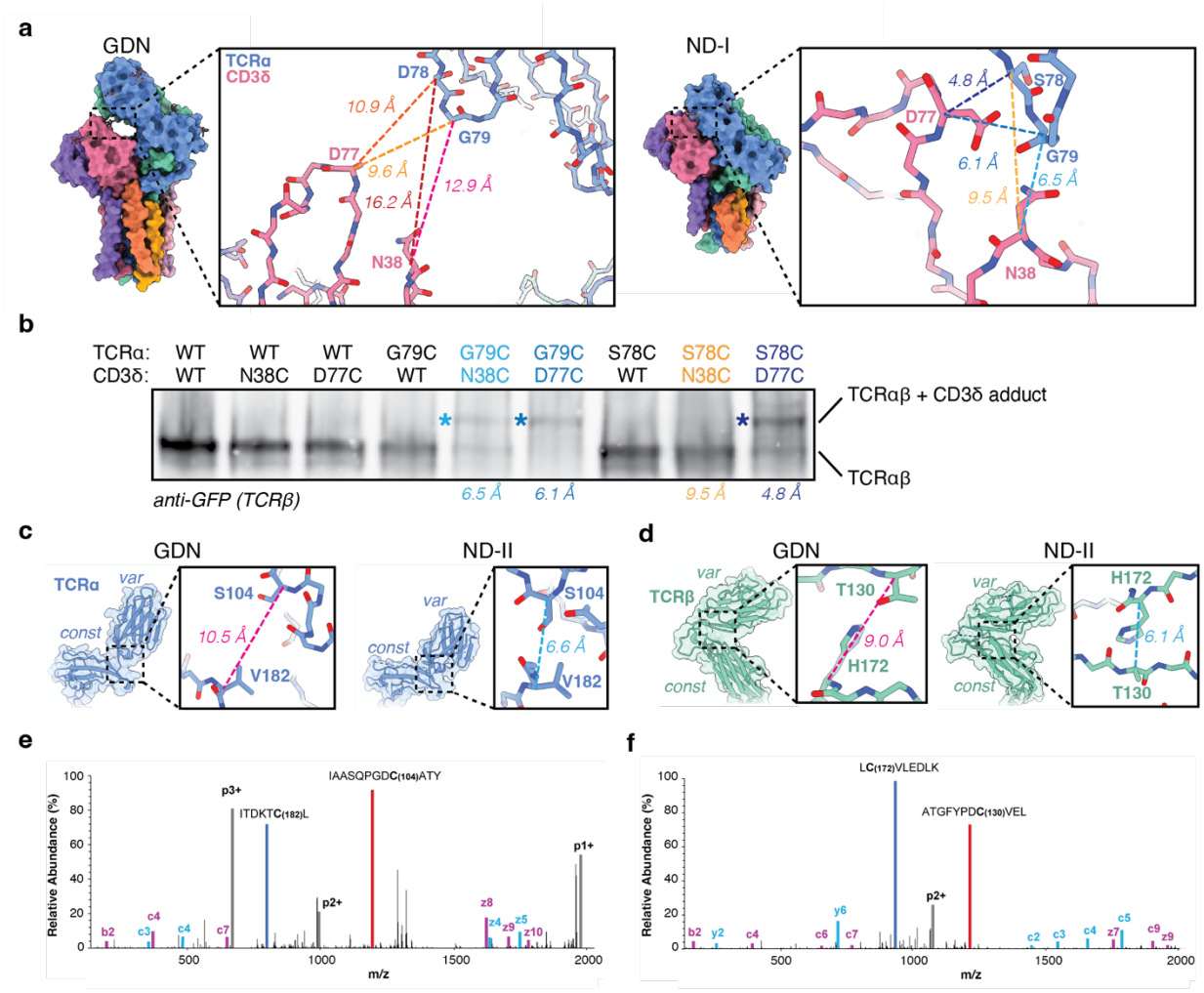

649

650 **Figure 4: Confirmation of the TCR–CD3 resting conformation *in situ.*** (a) Comparison of
651 Cα-Cα distances between apposing faces of CD3δ and TCRα in detergent and in a lipid bilayer,
652 highlighting plausible engineered disulfide positions in ND-I (distances in blue shades) that are
653 not geometrically plausible in GDN (distances in yellow, orange, red, magenta). (b) Non-
654 reducing SDS-PAGE gel of whole-cell lysates from HEK293T cells infected with the indicated
655 TCR–CD3 virus genotypes Western blotted for EGFP-tagged TCRβ. Engineered disulfides
656 yielding a TCRαβ–CD3δ covalent adduct resulted in an upward gel shift (asterisks). Color
657 coding and distances as in panel a. (c,d) Design of intrachain disulfides in the closed
658 conformation of TCRα (c) and TCRβ (d). Distances color coded as above. (e,f) Mass
659 spectrometric detection of intrachain disulfides in TCRα (e) and TCRβ (f). EThcD fragment
660 spectra of disulfide-linked dipeptides are shown. Gas-phase reduced linear peptides are shown
661 in red (peptide A) and blue (peptide B) with the reduced Cys highlighted in bold. Fragment ions
662 of the two linear peptides are shown in magenta (fragments of peptide A) and cyan (fragments
663 of peptide B). Charge-reduced precursor ions are shown in gray.
664
665

Figure 5

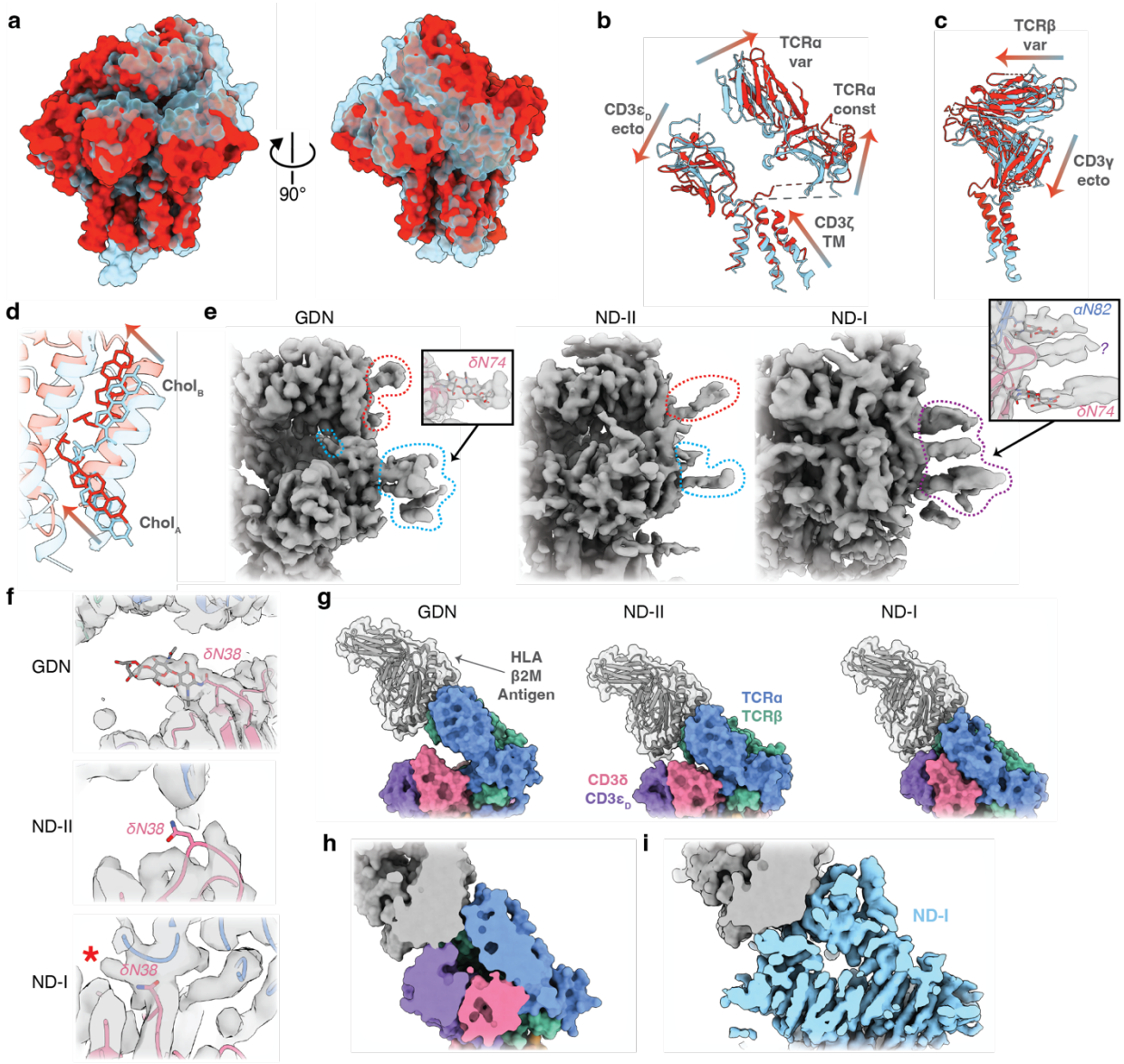
a
90°
b
TCRα
var
TCRα
const
CD3εD
ecto
CD3ζ
TM
c
TCRβ
var
CD3γ
ecto
d
CholB
CholA
e
GDN
ND-II
ND-I
δN74
αN82
?
δN74
f
GDN
δN38
ND-II
δN38
ND-I
δN38
g
GDN
ND-II
ND-I
HLA
β2M
Antigen
TCRα
TCRβ
CD3δ
CD3εD
h
i
ND-I

672 **Figure 5: Basal conformational variability of the TCR–CD3.** (a) Comparison of ND-I
673 (transparent cyan) and ND-II (red), shown here as model surfaces, aligned on the TCRα
674 transmembrane helix. (b,c) Gradient arrows highlight the domain movements underlying the
675 transition between ND-I (cyan) and ND-II (red). (d) TCRβ and CD3γ TM helix movement away
676 from the cholesterol-binding site during the transition from ND-I to ND-II, with arrows indicating
677 the accompanying movements of the cholesterols in the sterol-binding groove. (e) Comparison
678 of the TCRα and CD3δ lateral glycosylation sites (red and cyan dashed lines, respectively) in
679 the density maps showing increasing ordering of the glycan array with ectodomain closure
680 (purple dashed line). Insets highlight modeled asparagine-linked glycan cores (or partial cores)
681 modeled into these densities in GDN and ND-I. (f) Comparison of the CD3δ N38 residue in
682 GDN, ND-II and ND-I. Grey surface is the locally refined, DeepEMhancer-sharpened cryo-EM
683 density. (g) Modeling HLA-β2M-antigen (grey) binding to the TCR in the indicated
684 conformations. (h) Cross section through the HLA-TCR interface in ND-I shows close
685 association of HLA and CD3ε_D, but no large clashes. (i) Similarly, modeling HLA onto the locally
686 refined, DeepEMhancer-sharpened ND-I density does not show any large clashes between HLA
687 and unmodelled density.
688
689

690 **Figure 6**
691

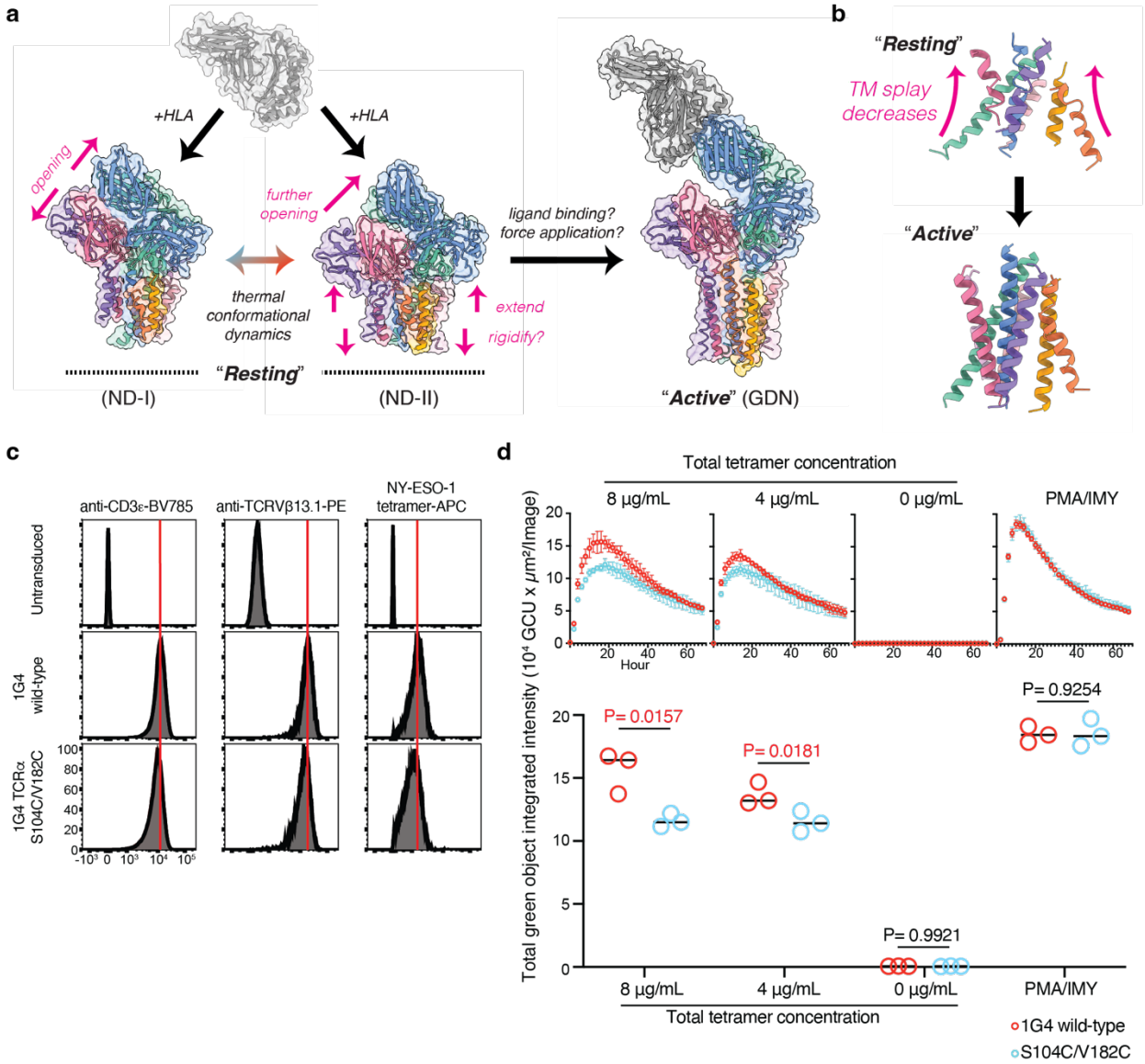

692
693
694
695

696 **Figure 6: Model of TCR–CD3 activation.** (a) Proposed model of TCR–CD3 conformational
697 dynamics. The unliganded TCR–CD3 explores resting subconformations (between ND-I and
698 ND-II). Ligand-induced activation is mediated by a conformational transition from ND-II to an
699 open, extended conformation, like in GDN. Magenta arrows and text indicate movements
700 required to transition to the next conformation in the series. (b) Changes in the TM helices
701 between hypothesized "resting" (ND-I shown) and "active" (GDN shown) conformations. (c)
702 Flow cytometry histogram from J8Zb2m-α-β- cells post tetramer-APC enrichment and stained
703 as indicated (n = 3 replicates). Cells were untransduced (top) or transduced with a virus
704 expressing the TCRαβ 1G4 genotype indicated (middle, bottom). Vertical axis is cell count
705 normalized to peak; horizontal axis is fluorescence in arbitrary units. Red line indicates
706 fluorescence intensity mode (histogram peak) for wild-type 1G4. (d) Time-dependent T-cell
707 activation quantified using an NFAT-ZsGreen reporter by live cell imaging. Top shows ZsGreen
708 fluorescence over time after addition of indicated concentrations of HLA-tetramer or
709 PMA/ionomycin for 1G4 wild-type (red) or TCRα S104C/V182C mutant-transduced cells (cyan).
710 Data shown are mean +/- standard deviation using biologic triplicates. Peak CD3-TCR
711 activation amplitudes are compared for each condition at the 8 μg/mL HLA-tetramer peak
712 (t=16h) for all HLA-tetramer concentrations or at the PMA/Ionomycin peak (t=10h) specifically
713 for that condition (bottom). P values calculated by unpaired, two-tailed t-test shown for each
714 comparison. $P < 0.05$ highlighted in red.
715

716 **Extended Data Figures and Legends**
717
718 **Extended Data Figure 1**
719

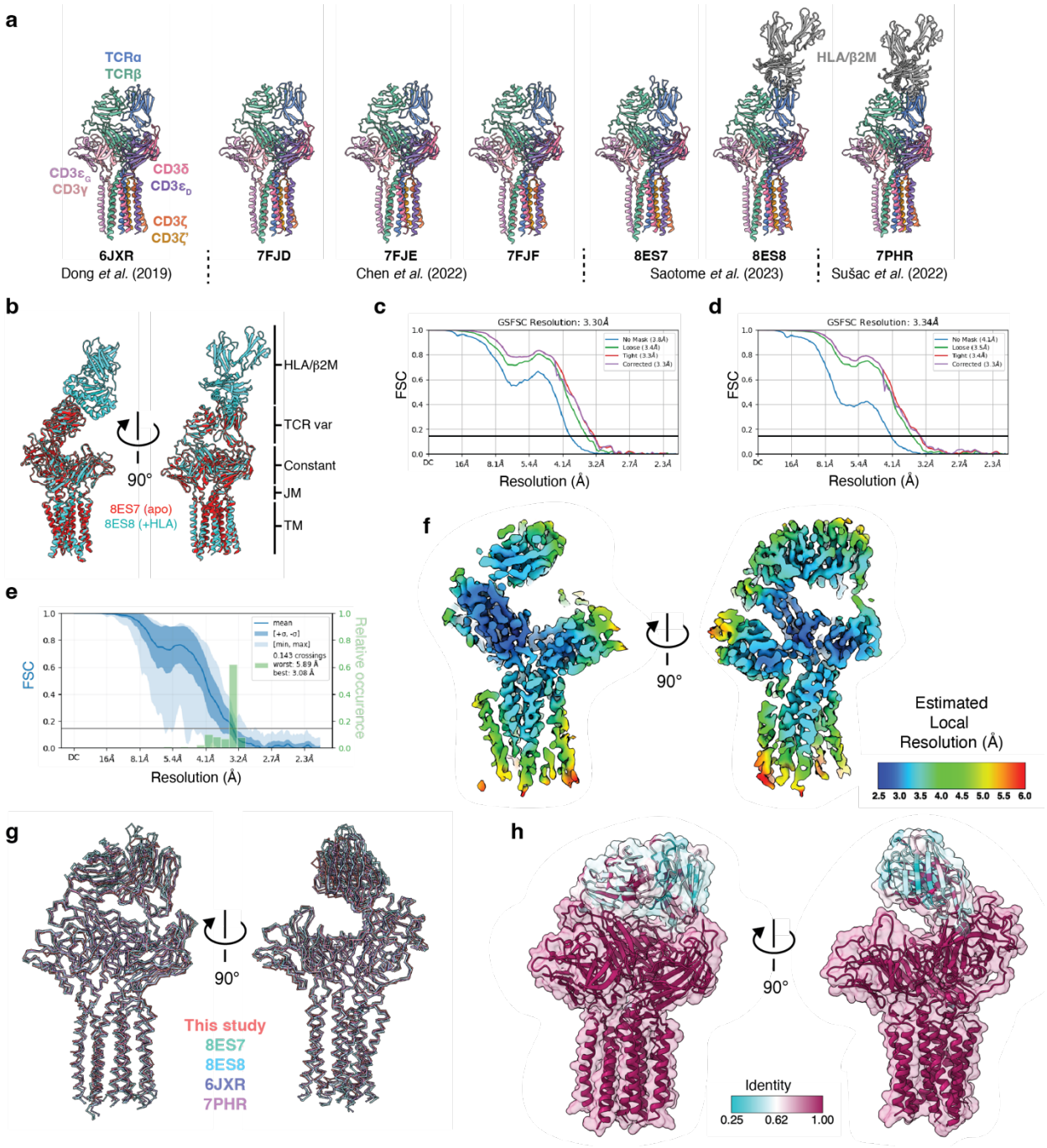

720
721
722
723

724 **Extended Data Figure 1: The TCR–CD3 in detergent.** (a) Cartoon representations of
725 previously published structures of the TCR–CD3 by itself and in complex with HLA-β2M-antigen
726 determined in detergent micelles by cryo-EM. Models are colored by chain as indicated. (b)
727 Superposition of published structures of a TCR–CD3 by itself (red) or in complex with HLA-β2M-
728 antigen (cyan), showing no meaningful structural change throughout the TCR structure upon
729 ligand binding. (c) Gold-standard Fourier shell correlation (FSC) curves for the map of the TCR–
730 CD3 in GDN (herein, simply "GDN") determined in this study after non-uniform refinement. (d)
731 FSC curve for the locally refined GDN map (mask excluded micelle density). While resolution
732 was not nominally improved by masking out the micelle, map interpretability was qualitatively
733 improved, and this map was used for further analysis. (e) Three-dimensional (3D) FSC analysis
734 for the locally refined GDN map, showing relatively little map anisotropy. (f) Central slices of the
735 locally refined GDN map, colored by local resolution estimate, as indicated in the panel. (g)
736 Backbone representation of the GDN structure compared with those of TCR–CD3 sequences
737 previously determined in other studies. Models containing HLA-β2M-antigen have had those
738 atoms removed for this analysis. (h) GDN model colored according to sequence identity among
739 the four TCR–CD3 sequences (this study and three priors) with cryo-EM structures determined
740 in detergent micelles.
741
742

743 **Extended Data Figure 2**

744

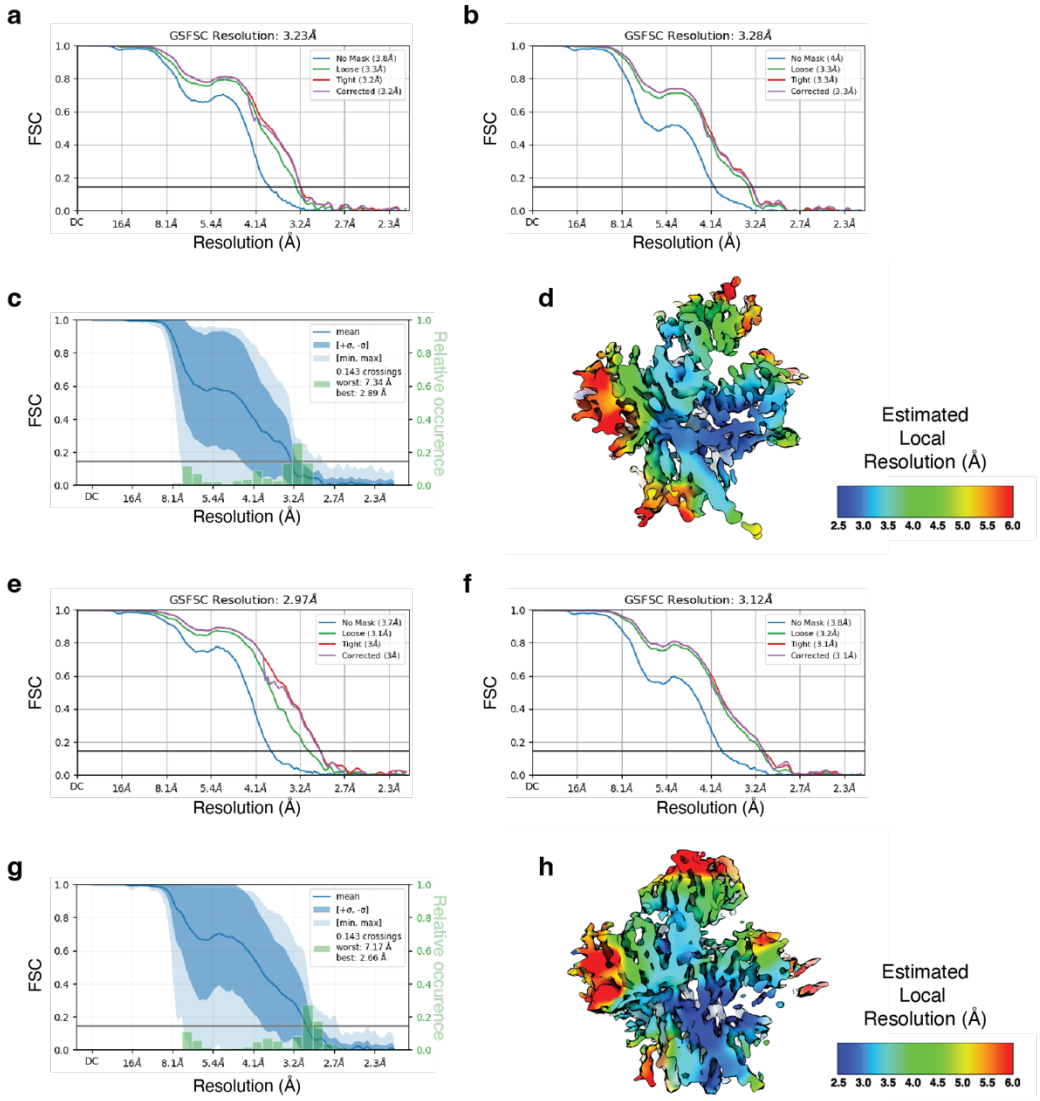

745
746
747
748

Extended Data Figure 2: Map assessment for ND-I and ND-II. (a) Gold-standard FSC curves for the ND-I map after non-uniform refinement. (b) FSC curves for the locally refined ND-I map (mask excluded nanodisc density). While resolution was not nominally improved by masking out the nanodisc, map interpretability was qualitatively improved, and this map was used for further analysis. (c) 3D FSC analysis for locally refined ND-I. Note the more extensive anisotropy than was seen for the TCR–CD3 in detergent micelles. (d) Central slice of locally refined ND-I, colored by local resolution estimate, as indicated in the panel. (e) Gold-standard FSC curves for the ND-II map after non-uniform refinement. (f) FSC curves for the locally refined ND-II map (mask excluded nanodisc density). As with ND-I, nominal resolution was not improved by masking out the nanodisc, but map interpretability was qualitatively improved, and this map was used for further analysis. (g) 3D FSC analysis for locally refined ND-II. Note again the more extensive anisotropy than was seen for the TCR in detergent micelles. (h) Central slice of locally refined ND-II, colored by local resolution estimate, as indicated in the panel.

764 **Extended Data Figure 3**

765

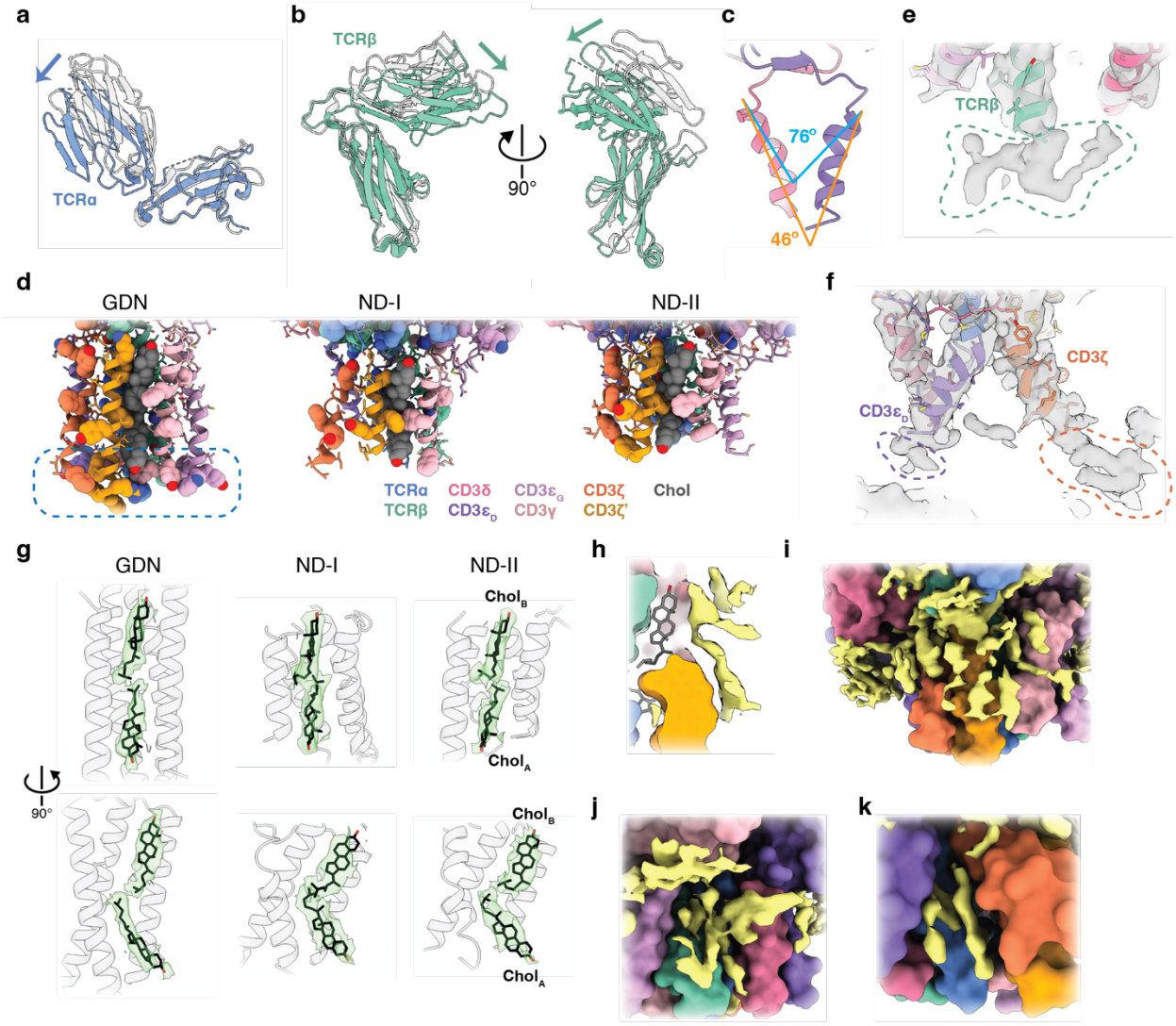

766
767
768
769

770 **Extended Data Figure 3: Structural detail of the TCR–CD3 in nanodiscs.** (a,b) Cartoon
771 representations of ND-I (solid) and GDN (transparent gray) TCRα (panel a) and TCRβ (panel b),
772 aligned to the respective TCR constant domains. Arrows indicate the movements of the variable
773 domains relative to the constant domains that comprise the "closure" of the variable domains in
774 ND-I/II relative to GDN. (c) The bent TM helices of the ND-I CD3ε_D heterodimer. Splay
775 measured at the level of the first helical turn (cyan) is greater than that of the helices overall
776 (orange). (d) Cartoon representation of the indicated models with basic and aromatic residues
777 highlighted as space-filling spheres. Blue dashed box highlights the clusters of basic and
778 aromatic residues modeled at the carboxy-termini of the TM helices in GDN, but unstructured in
779 ND-I and ND-II. Color legend applies to all figure panels. (e,f) Density projecting from the
780 carboxy-termini of the TM helices modeled in ND-II that could not be confidently modeled, but
781 likely corresponding to continuation of the polypeptide chains. Grey, DeepEMhancer-sharpened
782 maps. Dashed lines encircle the densities in question. (g) Density corresponding to the
783 cholesterols modeled in ND-I, ND-II, and GDN. The transparent green surface is the indicated
784 locally refined, B-factor-sharpened cryo-EM map, cropped to a zone of 2.2 Å around the
785 cholesterols (black). (h-k) Additional densities likely attributable to lipids in the ND-II map.
786 Proteins are shown as model surfaces, and cholesterol in stick representation. Yellow surface is
787 the ND-II B-factor-sharpened map after local refinement (h) or non-uniform refinement (i-k) with
788 the modeled densities subtracted to highlight unmodeled densities.
789
790

Extended Data Figure 4

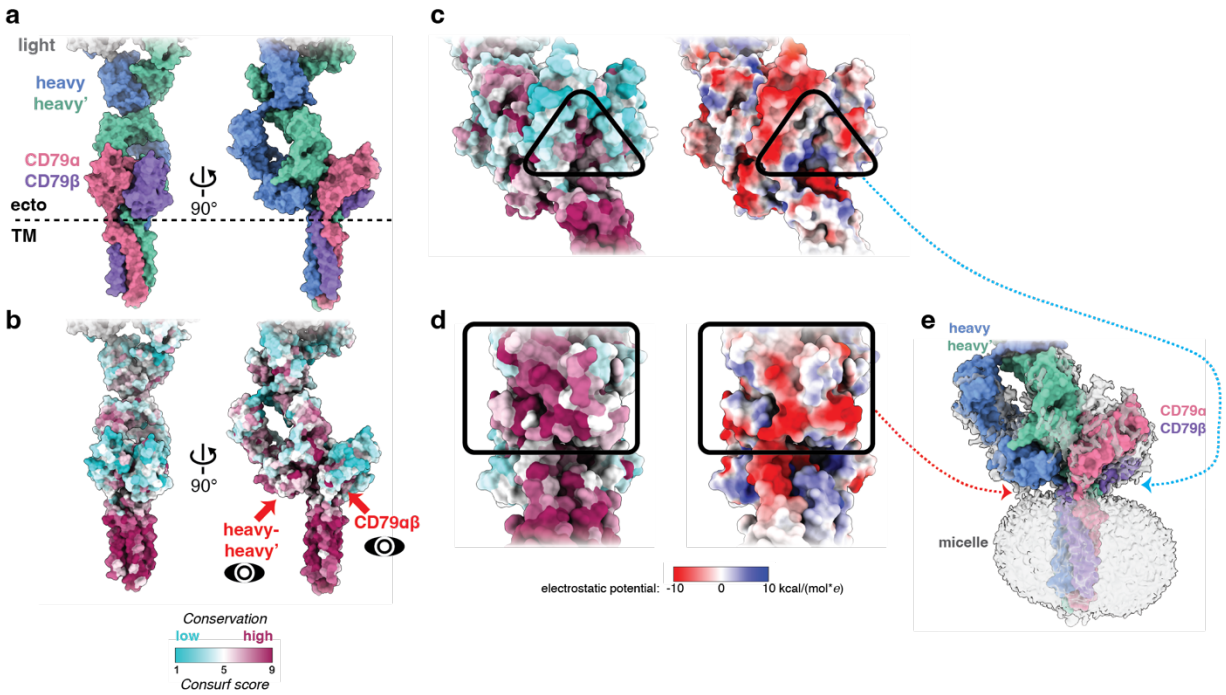

797 **Extended Data Figure 4: Insights into BCR structure and membrane interaction.** (a,b)
798 Surface representation of the human B-cell receptor (BCR) model, as determined in a detergent
799 micelle by cryo-EM (PDB 7XQ8)[23]. The model is colored by chain (a) and by sequence
800 conservation (b, scale applies to remainder of figure). Red arrows and eye icons labeled
801 CD79αβ and heavy-heavy' indicate the direction for the magnified views in panels (c) and (d),
802 respectively. (c) Membrane-proximal face of the CD79αβ interface, colored by conservation
803 (left, as in panel a) and electrostatic potential (right). Black triangle highlights region of high
804 sequence conservation and corresponding surface electropositivity. However, this patch is
805 oriented away from the micelle surface in the structure in detergent (dashed arrow to panel e).
806 (d) Membrane-proximal face of the IgM heavy chains, with black box highlighting broad
807 sequence conservation and largely electronegative conserved face. Dashed arrow indicates
808 contact between this surface patch and the detergent micelle density in panel e. Electrostatic
809 potential scale applies to panels c and d. (e) Surface model of the BCR with the unmodeled
810 map density shown (transparent gray). Note the detergent micelle enshrouding the TM helices
811 and making contact with the electronegative heavy-heavy' interface (red dashed arrow) but not
812 the electropositive CD79αβ interface (blue dashed arrow), which is the opposite of what might
813 be expected in a phospholipid membrane.
814
815

816 **Extended Data Figure 5**
817

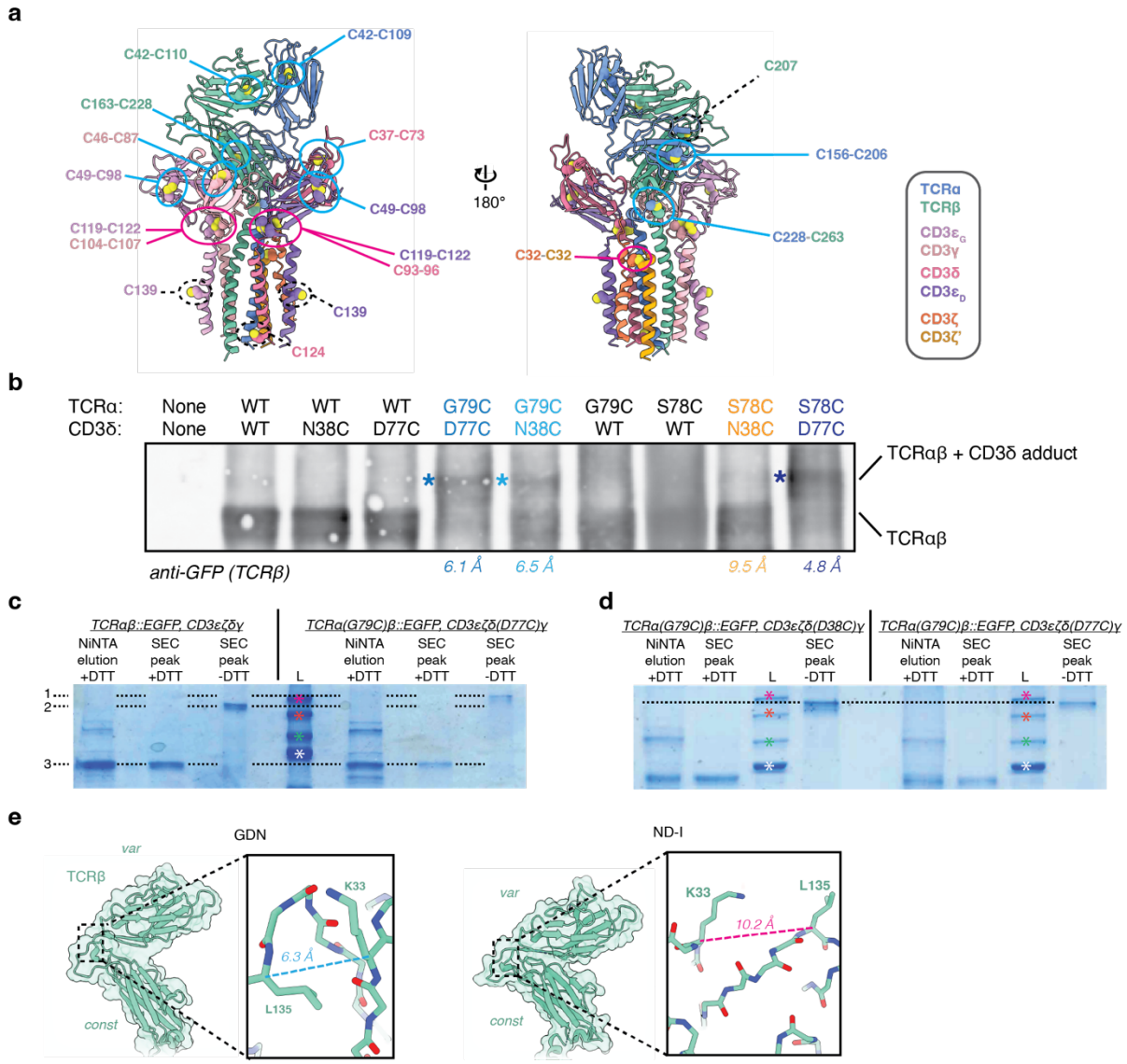

818
819
820
821

822 **Extended Data Figure 5: Engineered disulfide crosslinking.** (a) Location of all native
823 disulfides (solid cyan and magenta ovals) and unpaired cysteines (dashed black ovals) in this
824 TCR construct. Disulfides indicated by cyan ovals are amenable to mass spectrometric
825 detection as peptide pairs after EThcD, whereas disulfides indicated by magenta ovals are not
826 unambiguously detectable by this approach, as they are C-X-X-C lariats or symmetric between
827 CD3ζ homodimers. Subunits colored as indicated to the right. (b) Non-reducing SDS-PAGE gel
828 of NiNTA-affinity-purified TCR complex from HEK293T cells infected with the indicated TCR
829 virus genotypes and Western blotted for EGFP-tagged TCRβ. Engineered disulfides yielding a
830 TCRαβ–CD3δ covalent adduct results in an upward gel shift (asterisks). Color coding and
831 distances as in Figure 4a,b. (c,d) Acquastain-stained SDS-PAGE gels of NiNTA-affinity-purified
832 TCR complex reconstituted into nanodiscs and purified by size-exclusion chromatography
833 (SEC). Virus genotypes indicated above gels. The presence (+) or absence (-) of reducing
834 agent dithiothreitol (DTT) in the sample-loading buffer is indicated. In panel c, dashed line
835 markers 1, 2, and 3 indicate the inferred electrophoretic mobility of the TCRαβ::EGFP–
836 CD3δ adduct, TCRαβ::EGFP, and TCRβ::EGFP, respectively. Note the mobility shift between
837 the nonreduced wild-type TCR complex and the non-reduced TCRα(G79C)–CD3δ(D77C)
838 mutant complex. Molecular weight ladder (L) is color-coded with magenta, orange, green, and
839 white asterisks denoting 250 kDa, 150 kDa, 100 kDa, and 75 kDa, respectively. In panel d, the
840 non-reduced TCRα(G79C)–CD3δ(D38C) mutant complex displays an electrophoretic mobility
841 similar to that of the non-reduced TCRα(G79C)–CD3δ(D77C) mutant complex, consistent with
842 engineered disulfide formation. (e) Design of an engineered disulfide bond plausible in the GDN
843 conformation but not in the closed ND-I conformation.
844
845
846

847 **Extended Data Figure 6**
848

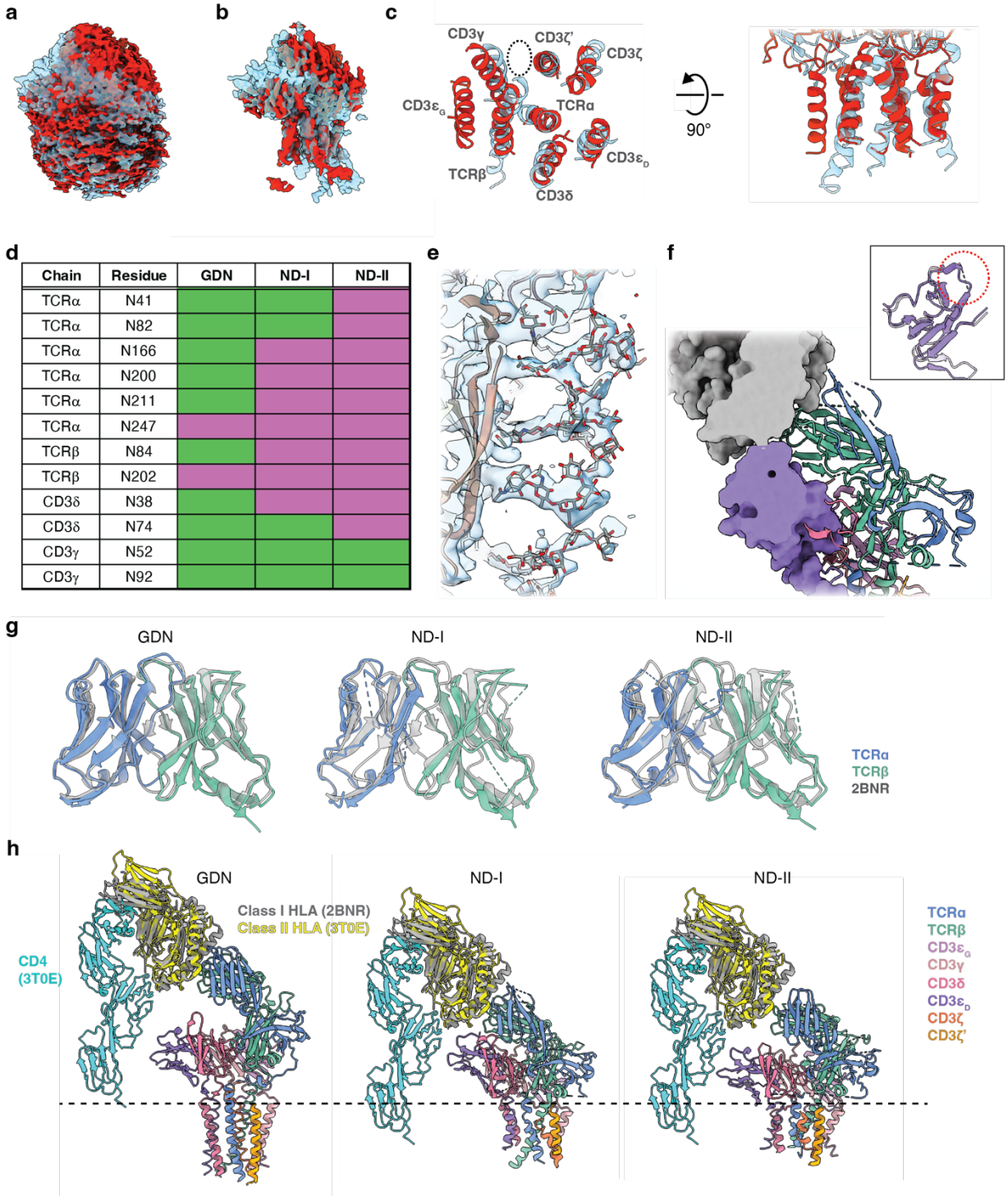

Chain	Residue	GDN	ND-I	ND-II
TCRα	N41			
TCRα	N82			
TCRα	N166			
TCRα	N200			
TCRα	N211			
TCRα	N247			
TCRβ	N84			
TCRβ	N202			
CD3δ	N38			
CD3δ	N74			
CD3γ	N52			
CD3γ	N92			

849
850
851

852 **Extended Data Figure 6: Basal conformational variation and glycosylation of the TCR–**
853 **CD3.** (a,b) Cryo-EM maps for ND-I (transparent cyan) and ND-II (solid red) aligned to the TCRα
854 transmembrane helix. The B-factor-sharpened map without local refinement and
855 DeepEMhancer-sharpened, locally refined maps are shown (a and b, respectively). (c) Relative
856 positions of the TM helices for ND-I and ND-II (colored as in panel a) viewed along the axis
857 perpendicular to the membrane plane (left) and parallel to the membrane (right). Dashed circle
858 indicates cholesterol-binding groove. (d) Graphical representation of partially modeled N-linked
859 glycans in GDN, ND-I, and ND-II. All asparagine residues within an N-X-S/T motif in the
860 structure are included in this list for completeness; however, TCRα N247 is located in the TM
861 domain and is unlikely to undergo glycosylation. Green, modeled; magenta, not modeled. (e)
862 Glycans (grey sticks) in a structured array on the surface of HIV Env as determined by x-ray
863 crystallography (PDB 5FYJ)[32]. Protein shown as cartoon backbone. 2Fo-Fc map contoured to
864 1σ and clipped to within 5 Å of the model. (f) Space-filling model of HLA docked onto ND-I with
865 the CD3ε_D ectodomain from GDN docked in place of that from ND-I, showing minimal, if any
866 steric clashing. Cartoon representation of the remainder of ND-I shown for orientation. Inset
867 shows alignment of CD3ε_D from GDN and ND-I by their ectodomains. Red dashed circle
868 highlights surface loop (residues 107-109) not modeled in ND-I (purple dashed line) but
869 modeled in GDN. (g) Alignment of TCR variable domains in this study to PDB 2BNR, a crystal
870 structure of the 1G4 TCR bound to HLA[26]. (h) Alignment of the CD4-Class II HLA-TCR ternary
871 complex structure (PDB 3T0E)[29] to the Class I HLA docked into the our structures as in panel F
872 and Figure 5. The Class II HLA from 3T0E is shown in yellow, and CD4 in cyan. Other color
873 coding as indicated in figure. Dashed black line represents the approximate boundary of the
874 lipid bilayer outer leaflet.

875 **Extended Data Tables**
876
877 **Extended Data Table 1: Model building and refinement statistics.**

	GDN	ND-I	ND-II
Model			
Composition (#)			
Chains	10	12	10
Atoms	8440 (Hydrogens: 0)	6460 (Hydrogens: 0)	6242 (Hydrogens: 0)
Residues	Protein: 1052 Nucleotide: 0	Protein: 836 Nucleotide: 0	Protein: 821 Nucleotide: 0
Water	0	0	0
Ligands	BMA: 3	BMA: 1	BMA: 1
	NAG: 15	NAG: 9	NAG: 3
	CLR: 2	CLR: 2	CLR: 2
Bonds (RMSD)			
Length (Å) (# > 4s)	0.003 (0)	0.004 (0)	0.003 (0)
Angles (degrees) (# > 4s)	0.923 (6)	0.855 (6)	0.906 (3)
MolProbity score	1.9	2.71	2.67
Clash score	13.57	21.05	18.43
Ramachandran plot (%)			
Outliers	0.1	0.26	0.4
Allowed	3.67	7.14	9.49
Favored	96.24	92.6	90.12
Rama-Z (Ramachandran plot Z-score, RMSD)			
whole (N = 1036)	0.51 (0.26)	-2.15 (0.27)	-1.91 (0.29)
helix (N = 214)	0.63 (0.34)	-1.96 (0.42)	-1.14 (0.41)
sheet (N = 286)	1.85 (0.32)	-0.40 (0.37)	0.54 (0.37)
loop (N = 536)	-0.64 (0.26)	-1.77 (0.26)	-2.35 (0.28)
Rotamer outliers (%)	0.56	3.72	2.99
Peptide plane (%)			
Cis proline/general	11.6/0.2	6.1/0.0	3.3/0.0
Twisted proline/general	0.0/0.1	0.0/0.0	0.0/0.3
CaBLAM outliers (%)	3.04	5.6	7.32
ADP (B-factors)			
Iso/Aniso (#)	8440/0	6460/0	6242/0
min/max/mean			
Protein	78.97/260.88/146.95	46.79/362.28/144.81	51.96/387.42/144.45
Nucleotide	---	---	---

Ligand	92.44/292.30/180.12	78.92/388.12/221.92	124.98/195.38/160.46
Water	---	---	---
Occupancy			
Mean	1	1	1
occ = 1 (%)	100	100	100
0 < occ < 1 (%)	0	0	0
occ > 1 (%)	0	0	0
Data			
Box			
Lengths (Å)	(88.56, 101.52, 138.24)	(95.04, 87.48, 110.16)	(92.88, 92.88, 101.52)
Supplied Resolution (Å)	3.3	3.3	3.1
Resolution Estimates (Å), Masked			
d FSC (half maps; 0.143)	3.4	3.2	3.1
d 99 (full/half1/half2)	4.3/3.3/3.3	4.5/3.7/3.7	4.2/3.4/3.4
d model	3.7	3.3	3.1
d FSC model (0/0.143/0.5)	3.2/3.3/3.8	3.2/3.4/7.4	3.1/3.3/7.2
Resolution Estimates (Å), Unmasked			
d FSC (half maps; 0.143)	3.5	3.3	3.1
d 99 (full/half1/half2)	4.3/2.5/2.5	4.5/3.5/3.4	4.2/3.2/3.2
d model	3.8	3.3	3.1
d FSC model (0/0.143/0.5)	3.3/3.4/3.8	3.2/3.5/7.6	3.1/3.4/7.3
Map min/max/mean	-0.60/1.36/0.06	-0.65/1.68/0.09	-0.67/1.77/0.10
Model vs. Data			
CC (mask)	0.82	0.57	0.59
CC (box)	0.81	0.65	0.68
CC (peaks)	0.7	0.41	0.48
CC (volume)	0.82	0.58	0.59
Mean CC for ligands	0.72	0.56	0.58

878

879 **Extended Data Table 2: Disulfide-linked peptides identified by cross-linking mass**
880 **spectrometry.** Disulfide-linked peptides identified for each TCR genotype. Peptides with an
881 XLinkX score greater than 30 are shown, as no native peptides were observed below this
882 threshold. Color coding as follows: green, expected native disulfide; cyan, expected engineered
883 disulfide; red, non-native disulfide or contaminant; magenta, off-target disulfide involving the
884 engineered cysteines.
885

	XLINKX SCORE	SEQUENCE 1	CHAIN 1	CYS 1	SEQUENCE 2	CHAIN 2	CYS 2
TCRα(WT), TCRβ(WT)							
	120.57	V[C]LATGFYPDHVEL	B	163	[C]QVQFY	B	228
	106.91	LT[C]DAEAK	G	46	GMYQ[C]K	G	87
	95.96	Q[C]AQDMNHEY	B	42	F[C]ASSY	B	110
	90.84	T[C]PQYPGSEILW	E	49	VN[C]NTSITW	D	37
	73.16	FPSPESS[C]DVK	A	228	AD[C]GFTSESY	B	263
	70.28	SVPEGENLVLN[C]SFTDSAIY	A	42	L[C]AVRPLY	A	109
	69.67	SNKSDFA[C]ANAF	A	206	SV[C]LF	A	156
	58.32	T[C]PQYPGSEILW	E	49	[C]QVQFY	B	228
	53.59	VFVN[C]NTSITW	D	37	GIYR[C]NGTDIY	D	73
	40.68	NNSIIPEDTFFPSPESS[C]DVK	A	228	ATLV[C]L	B	163
	30.56	T[C]PQYPGSEILW	E	49	YV[C]YPR	E	98
TCRα(S104C-V182C), TCRβ(WT)							
	120.8	LT[C]DAEAK	G	46	GMYQ[C]K	G	87
	106.26	V[C]LATGFYPDHVEL	B	163	R[C]QVQFY	B	228
	104.38	Q[C]AQDMNHEY	B	42	F[C]ASSY	B	110
	92.7	GIYR[C]NGTDIYK	D	73	VFVN[C]NTSITW	D	37
	80.51	SVPEGENLVLN[C]SFTDSAIY	A	42	L[C]AVRPLY	A	109
	78.49	SNKSDFA[C]ANAF	A	206	SV[C]LF	A	156
	72.7	T[C]PQYPGSEILW	E	49	[C]QVQFY	B	228
	72.62	IAASQPGD[C]ATY	A	104	ITDKT[C]LDMR	A	182
	70.28	SVPEGENLVLN[C]SFTDSAIY	A	42	[C]NGTDIY	D	73
	65.27	V[C]LATGFYPDHVEL	B	163	T[C]PQYPGSEILW	E	49
	60.55	SDFA[C]ANAF	A	206	ITDKT[C]L	A	182
	56.37	FPSPESS[C]DVK	A	228	AD[C]GFTSESY	B	263
	49.26	ITDKT[C]L	A	182	SV[C]LF	A	156
	48.23	T[C]PQYPGSEILW	E	49	VN[C]NTSITW	D	37
	45.66	T[C]PQYPGSEILW	E	49	YV[C]YPR	E	98
TCRα(WT), TCRβ(T130C-H172C)							
	99.32	QEDGSVLLT[C]DAEAK	G	46	GMYQ[C]KGSQNK	G	87
	96.82	Q[C]AQDMNHEY	B	42	F[C]ASSY	B	110
	88.95	FGEGSRL[C]VLEDLK	B	130	ATGFYPD[C]VELSW	B	172
	79.2	SNKSDFA[C]ANAF	A	206	SV[C]LF	A	156
	72.18	SVPEGENLVLN[C]SFTDSAIY	A	42	L[C]AVRPLY	A	109
	71.14	GIYR[C]NGTDIYK	D	73	VFVN[C]NTSITW	D	37
	63.42	L[C]VLEDLK	B	130	LT[C]DAEAK	G	46
	62.17	L[C]VLEDLK	B	130	SV[C]LF	A	156
	54.2	L[C]VLEDLK	B	130	F[C]ASSY	B	110
	53.77	T[C]PQYPGSEILW	E	49	L[C]VLEDLK	B	130

53.5	FPSPESS[C]DVK	A	228	AD[C]GFTSESY	B	263
47.92	T[C]PQYPGSEILW	E	49	[C]QVQFY	B	228
41.91	L[C]VLEDLK	B	130	[C]QVQFY	B	228
41.51	AD[C]GFTSESY	B	263	L[C]VLEDLK	B	130
38.79	T[C]PQYPGSEILW	E	49	YV[C]YPR	E	98
36.32	ATGFYPD[C]VEL	B	172	[C]LSSR	B	207
34.92	VFVN[C]NTSITW	D	37	GMYQ[C]K	G	87
30.54	LT[C]DAEAK	G	46	[C]QVQFY	B	228
TCRα(WT), TCRβ(K33C-L135C)						
96.43	GIYR[C]NGTDIYK	D	73	VFVN[C]NTSITW	D	37
95.43	LT[C]DAEAK	G	46	GMYQ[C]K	G	87
90.79	ATLV[C]LATGFYPDHVEL	B	163	R[C]QVQFY	B	228
81.71	LTVLED[C]K	B	135	ATLV[C]L	B	163
81.57	Q[C]AQDMNHEY	B	42	F[C]ASSY	B	110
81.57	LTVLED[C]K	B	135	[C]QVQFY	B	228
79.2	SNKSDFA[C]ANAF	A	206	SV[C]LF	A	156
76.07	T[C]PQYPGSEILW	E	49	[C]QVQFY	B	228
72.9	SVPEGENLVLN[C]SFTDSAIY	A	42	L[C]AVRPLY	A	109
69.49	LTVLED[C]K	B	135	F[C]ASSY	B	110
65.27	V[C]LATGFYPDHVEL	B	163	T[C]PQYPGSEILW	E	49
64.22	ATLV[C]LATGFYPDHVEL	B	163	ATLV[C]LATGFYPDHVEL	B	163
53.91	T[C]PQYPGSEILW	E	49	VN[C]NTSITW	D	37
48.05	V[C]LATGFYPDHVEL	B	163	SDFA[C]ANAF	A	206
47.05	LTVLED[C]K	B	135	SV[C]LF	A	156
45.66	V[C]LATGFYPDHVEL	B	163	SV[C]LF	A	156
43.9	T[C]PQYPGSEILW	E	49	V[C]YPR	E	98
36.08	FPSPESS[C]DVK	A	228	AD[C]GFTSESY	B	263
35.13	T[C]PQYPGSEILW	E	49	LTVLED[C]K	B	135
35.04	T[C]PQYPGSEILW	E	49	[C]AVRPL	A	109
34.06	V[C]LATGFYPDHVEL	B	163	VLN[C]SFTDSAIY	A	42
30.82	SDFA[C]ANAF	A	206	LTVLED[C]K	B	135

886